The Astrophysical Journal, 937:36 (22pp), 2022 September 20 https://doi.org/10.3847/1538-4357/ac8b11

Chemical Diversity in Protoplanetary Disks and Its Impact on the Formation History of Giant Planets

Elenia Pacetti[1,2], Diego Turrini[1,3], Eugenio Schisano[1], Sergio Molinari[1], Sergio Fonte[1], Romolo Politi[1], Patrick Hennebelle[4], Ralf Klessen[5,6], Leonardo Testi[4,7], and Ugo Lebreuilly[4]
[1] INAF—Istituto di Astrofisica e Planetologia Spaziali (INAF-IAPS), Via Fosso del Cavaliere 100, I-00133, Rome, Italy; elenia.pacetti@inaf.it
[2] Dipartimento di Fisica, Sapienza Università di Roma, Piazzale Aldo Moro 2, I-00185, Rome, Italy
[3] INAF—Osservatorio Astrofisico di Torino, Via Osservatorio 20, I-10025, Pino Torinese (TO), Italy
[4] AIM, CEA, CNRS, Université Paris-Saclay, Université Paris Diderot, Sorbonne Paris Cité, F-91191, Gif-sur-Yvette, France
[5] Universität Heidelberg, Zentrum für Astronomie, Institut für Theoretische Astrophysik, Albert-Ueberle-Str. 2, D-69120, Heidelberg, Germany
[6] Universität Heidelberg, Interdisziplinäres Zentrum für Wissenschaftliches Rechnen, INF 205, D-69120, Heidelberg, Germany
[7] ESO—European Southern Observatory, Karl-Schwarzschild-Strasse 2, D-85748, Garching bei München, Germany
Received 2022 May 7; revised 2022 August 10; accepted 2022 August 16; published 2022 September 22

Abstract

Giant planets can interact with multiple and chemically diverse environments in protoplanetary disks while they form and migrate to their final orbits. The way this interaction affects the accretion of gas and solids shapes the chemical composition of the planets and of their atmospheres. Here we investigate the effects of different chemical structures of the host protoplanetary disk on the planetary composition. We consider both scenarios of molecular (inheritance from the prestellar cloud) and atomic (complete chemical reset) initial abundances in the disk. We focus on four elemental tracers of different volatility: C, O, N, and S. We explore the entire extension of possible formation regions suggested by observations by coupling the disk chemical scenarios with *N*-body simulations of forming and migrating giant planets. The planet formation process produces giant planets with chemical compositions significantly deviating from that of the host disk. We find that the C/N, N/O, and S/N ratios follow monotonic trends with the extent of migration. The C/O ratio shows a more complex behavior, dependent on the planet accretion history and on the chemical structure of the formation environment. The comparison between S/N^* and C/N^* (where * indicates normalization to the stellar value), constrains the relative contribution of gas and solids to the total metallicity. Giant planets whose metallicity is dominated by the contribution of the gas are characterized by $N/O^* > C/O^* > C/N^*$ and allow to constrain the disk chemical scenario. When the planetary metallicity is instead dominated by the contribution of the solids we find that $C/N^* > C/O^* > N/O^*$.

Unified Astronomy Thesaurus concepts: Protoplanetary disks (1300); Extrasolar gaseous giant planets (509); Abundance ratios (11); Planetary atmospheres (1244); Planet formation (1241); Metallicity (1031); Exoplanet atmospheric composition (2021); Chemical abundances (224); Astrochemistry (75)

Supporting material: animation

1. Introduction

The past decade has witnessed a huge growth in our knowledge and comprehension of exoplanetary systems, paving the way for a more systematic study of the initial stages of their evolution. Such growth has been achieved thanks to the improved resolution of modern observational facilities. For instance, observations performed with ALMA allowed for the first direct detection of gaps and rings in the gas and dust of protoplanetary disks, which are thought to be the signature of forming giant planets (e.g., ALMA Partnership et al. 2015; Isella et al. 2016; Fedele et al. 2017; Andrews et al. 2018; Fedele et al. 2018 and references therein; Long et al. 2018; Pinte et al. 2018; Currie et al. 2022). Improvements in the characterization of the chemical structure of disks have been made as well, allowing for the first direct comparison between the volatile inventory of extrasolar systems and the solar system records (Bianchi et al. 2019; Drozdovskaya et al. 2019; Öberg & Bergin 2021). Such new evidence combines with the information provided by population studies of exoplanets aimed at investigating the architectures and characteristics of the more than 5000 exoplanets identified to date. The overall emerging picture is that the characteristics of planets (their occurrence, formation pathway, orbital architecture, final mass, and composition) are extremely diverse and uniquely shaped by the physical and chemical properties of the environment in which they formed (e.g., Madhusudhan 2019; Zhu & Dong 2021 and references therein).

Among the wide variety of worlds discovered so far, giant planets attract considerable interest due to the role they play in shaping the architectures of planetary systems and for their influence on terrestrial planet formation (Raymond et al. 2014; Sotiriadis et al. 2018; Drazkowska et al. 2022). Our understanding of such planets will soon take a big step forward, thanks to the observations by next-generation telescopes such as JWST and ELT. Moreover, giant planets will be the main target of the upcoming Ariel space mission (Tinetti et al. 2018; Turrini et al. 2018; Edwards et al. 2019a).

Comparative studies between giant planets in exoplanetary systems and in the solar system revealed an unexpected diversity in their orbital architectures. Specifically, giant planets are found to cover a wide range of orbital radii, between 0.01 and 100 au.[8] Although the detection of giant

[8] The Extrasolar Planets Encyclopaedia, http://www.exoplanet.eu.

planets far from the star does not raise particular concerns, their existence within 0.1 au poses a great challenge to understanding their formation history. In particular, neither the core accretion (Pollack et al. 1996) nor the gravitational instability (Boss et al. 2000) models, allow a giant planet to form in situ and very close to the star. Therefore, such planets must have migrated inward from their original formation location to the current one.

What clearly emerges from this result is that the final orbit is simply the end point of the formation process of a giant planet. As such, its properties do not put any constraint on the planet's birthplace and migration history. Instead, Öberg et al. (2011) suggested that this information is locked into the final composition of the planet's atmosphere. Such an idea is motivated by the fact that giant planets are expected to form by accreting gas and planetesimals from the surrounding protoplanetary disk. In this regard, migration allows planets to visit regions of the disk with different chemical compositions, as set by the thermal structure of the disk itself. As the chemical abundances in the planet's atmosphere are expected to reflect the composition of the accreted material, they can effectively be used as a proxy for the formation and migration pathways of the planet. A detailed description of how this can be implemented into models of giant planet formation can be found in Turrini et al. (2021), which we refer to as Paper I hereafter, and is summarized in the Appendix.

In Paper I we simulated the formation and migration of a giant planet in a protoplanetary disk. By focusing on four elemental tracers in the final atmosphere of the planet, namely carbon (C), oxygen (O), nitrogen (N), and sulfur (S), we built a model to constrain the extent of the migration and the phase of the accreted material. We employed a stationary protoplanetary disk that inherited the composition from its parent cloud. However, a complete picture of the physical and chemical structure of protoplanetary disks is still elusive. One of the still open questions concerns precisely their initial chemical setup. Specifically, it is unclear whether disks inherit their composition from the prestellar phase (i.e., from the molecular cloud out of which the host star formed, as assumed in Paper I), in the so-called *inheritance* scenario, or experience a complete chemical reset as a result of ionizing irradiation from the protostar, known as *reset* scenario. To date, neither the inheritance nor the reset scenario can completely explain the solar system record. In fact, comparative studies of meteorites and comets in the solar system with protostellar objects in protoplanetary disks provide evidence for both of them (e.g., Öberg & Bergin 2021 and references therein).

In this work, we tested the diagnostic power of our model against different initial chemical conditions for the protoplanetary disk. To further explore the parameter space, we also examined the implications of different levels of ionizing radiation reaching the disk midplane.

Section 2 provides a description of our planet formation and disk compositional models, further discussed also in the Appendix. In Section 3 we present our results in terms of elemental ratios in the disk and in the planet envelope. Specifically, we discuss how the elemental ratios can be used to characterize giant planets in terms of their accretion history (Section 3.3), migration scenario (Section 3.4), and chemical structure of the birth environment (Section 3.5). Finally, in Section 4, we draw the conclusions of our work and summarize the applications of our results.

Table 1
Parameters of the Disk Model

Disk	
Stellar mass	1 $M_\odot$
Inner disk radius	0.1 au
Outer disk radius	500 au
Disk mass	0.053 $M_\odot$
Disk temperature	280 K at 1 au
Planetesimals	
Radius	50 km
Density: rock dominated	2.4 g cm^{-3}
Density: ice dominated	1 g cm^{-3}
Distribution	1–150 au

2. Numerical and Compositional Model

Paper I studied the link between giant planet formation and composition by coupling a description of the native circumstellar disk, assuming chemical inheritance by the native cloud, with detailed *N*-body simulations of the formation and migration of a giant planet in a dynamically evolving disk of gas and planetesimals. While migrating through different compositional regions of the disk, the planet accretes gas and planetesimals, whose mixture sets the composition of the giant planet and of its extended atmosphere. In this work, we expand the analysis of Paper I by coupling the outcome of its original simulations with four compositional models for gas and solids in protoplanetary disks. Details on the adopted disk model and on the physical processes and dynamical effects modeled by the simulations are provided in Sections 2.1 and 2.2. Further details on the planet formation model can also be found in the Appendix. Section 2.3 is dedicated to the modeling of the disk ionization environment. The four compositional models of the protoplanetary disk are described in Section 2.4.

2.1. Disk Model: Gas and Planetesimals

The protoplanetary disk considered in Paper I and in this work is modeled over the observed disk HD 163296 (Isella et al. 2016; Turrini et al. 2019). The gas surface density and temperature profiles of HD 163296 were rescaled to match the total disk mass and the estimated temperature profile of the Minimum Mass Solar Nebula (MMSN; Hayashi 1981). The physical parameters of the resulting disk are summarized in Table 1. Our disk model assumes radial profiles of gas surface density and temperature on the midplane that are constant in time and parameterized as:

$$\Sigma_{\rm gas}(r) = \Sigma_0 \left(\frac{r}{165\ {\rm au}}\right)^{-0.8} \exp\left[-\left(\frac{r}{165\ {\rm au}}\right)^{1.2}\right] \quad (1)$$

$$T(r) = T_0 \left(\frac{r}{1\ {\rm au}}\right)^{-1/2}, \quad (2)$$

where $\Sigma_0 = 3.3835$ g cm^{-2} and $T_0 = 280$ K.

Regarding the solid component of the disk, we assumed that it is distributed between 1 and 150 au with a surface density profile:

$$\Sigma_{\rm solids}(r) = \begin{cases} 2\, Z_i(r)\, \Sigma_{\rm gas}(r) & x \leqslant 150\ {\rm au} \\ 0 & x > 150\ {\rm au}, \end{cases} \quad (3)$$

where $Z_i(r)$ is the mass fraction of condensed material. A factor of 2 was introduced as a concentration factor to account for the inward drift of dust and pebbles as a consequence of their dynamical coupling with the gas (see Paper I and references therein for further discussion).

Following the approach of Paper I, we assumed that the bulk of dust in the disk is rapidly converted into planetesimals over a timescale of 1 Myr, as suggested by comparisons between the masses of exoplanetary systems and of the dust and gas in protoplanetary disks (e.g., Manara et al. 2018; Mulders et al. 2021). The assumption is also consistent with recent observations of dust temporal evolution in disks (see Testi et al. 2022 and Bernabò et al. (2022) for further discussion) and with meteoritic data from the solar system (e.g., Scott 2007; Lichtenberg et al. 2022, and references therein).

The conversion of dust into planetesimals reduces the efficiency of the gas–grain chemistry, hence slowing down the chemical evolution of the disk itself. When the disk is severely depleted in dust with respect to the initial stages of its evolution, its chemical composition can be reasonably approximated as fixed. We then assumed that the composition of our disk evolves until 1 Myr and remains fixed thereafter (see Section 2.4 for details on the compositional model). The implications of physically and chemically evolving disks will be explored in future works.

The planetesimals in our model are all characterized by a fixed radius of $r_p = 50$ km (Klahr & Schreiber 2016; Johansen & Lambrechts 2017) and are divided into two populations, depending on whether they are located within or beyond the water snowline. Planetesimals inside the water snowline are rock dominated and characterized by a density of $\rho_{\rm rock} = 2.4\ {\rm g\,cm^{-3}}$, while those beyond the water snowline are enriched in ices and characterized by a density of $\rho_{\rm ice} = 1\ {\rm g\,cm^{-3}}$. See the Appendix for further discussion.

The radius and density values are used to compute the effects of gas on the planetesimal dynamics. All the planetesimals evolve dynamically under the influence of both the forming giant planet and the disk itself. Specifically, the planetesimals interact gravitationally with the forming giant planet, whose collisional cross section determines whether planetesimals are accreted or scattered by planetary encounters. Moreover, at each location in the disk the planetesimals are subject to two competing forces: the dynamical excitation due to the disk self-gravity and the damping effect of the gas drag. The implementation of the disk self-gravity is based on the analytical treatment for thin disks by Ward (1981), following the approach of Marzari (2018) and Nagasawa et al. (2019). The effect of the gas drag on the dynamical evolution of the planetesimals is modeled following the treatment by Brasser et al. (2007), with the updated drag coefficients from Nagasawa et al. (2019). See Paper I and references therein for more details.

The planetesimal disk is simulated by means of a set of dynamical tracers distributed randomly between 1 and 150 au with a uniform probability distribution and a spatial density of 2000 tracers/au. Each tracer represents a swarm of planetesimals. The mass of the swarm is computed by dividing the total solid mass in an annular region of the disk (computed by integrating Equation (3)) by the number of dynamical tracers it contains. One can then associate the flux of impacting tracers recorded by the simulations with a mass flux of accreted planetesimals on the giant planet (see Paper I for details).

In Figure 1, the first four panels from the top are snapshots of the *N*-body simulations showing the dynamical evolution of the planetesimals at different stages of the planet formation and migration history. As the planet forms and migrates, planetesimals from different compositional regions of the disk are dynamically excited and end up being scattered or accreted onto the planet. An example of the normalized flux of accreted planetesimals is shown by the blue curve in the bottom-right panel of Figure 1. See Paper I and the Appendix for more details.

2.2. Formation and Migration Model

The *N*-body simulations were performed with MERCURY-ARχES (Turrini et al. 2019, 2021), a high-performance implementation of the hybrid symplectic algorithm of the MERCURY 6 software from Chambers (1999). Besides the improvements in numerical stability and computational efficiency with respect to MERCURY, the algorithm of MERCURY-ARχES allows for simulating the mass growth, the radius evolution, and the orbital migration at each stage of giant planet formation, as well as the effects of the disk self-gravity and of the gas drag. We refer the reader to Paper I and the Appendix for more details on the theoretical treatment of these processes and on their numerical implementation in the *N*-body simulations. In the following, we provide a brief overview of what is included in the planet formation and migration model.

We simulated a giant planet that forms and migrates on the disk midplane (i.e., on an orbit with inclination $i = 0$) over a timescale of 3 Myr, growing from a planetary embryo to a Jupiter-like giant planet. We adopted a two-phase approach to model both the mass growth and the evolution of the physical radius of the planet, following the growth tracks from Lissauer et al. (2009); Bitsch et al. (2015), and D'Angelo et al. (2021) using the parametric approach from Turrini et al. (2011, 2019). In the first 2 Myr, the planet accretes its core and extended atmosphere and grows from an initial mass of $M_0 = 0.1\,M_\oplus$ (mass of the planetary embryo) to a critical mass of $M_c = 30\,M_\oplus$, equally shared between the core and the atmosphere. In this phase, the physical radius of the planet grows following the approach described by Fortier et al. (2013), which is based on the hydrodynamical simulations by Lissauer et al. (2009). Over the last 1 Myr, the planet undergoes its runaway gas accretion phase and its mass grows until the final value of $M_F = 317.8\,M_\oplus$ (equal to 1 Jovian mass) is reached. At the onset of the runaway gas accretion, the physical radius of the planet starts to shrink due to the gravitational infall of the gas, reaching a final value of $R_I = 1.15 \times 10^5$ km (equal to 1.6 Jovian radii). An example of the mass growth track normalized to its final value is shown in the bottom-right panel of Figure 1 (orange curve) for the case of a giant planet that starts forming at 19 au.

To model the migration of the giant planet we adopted the realistic nonisothermal migration tracks from the population synthesis models by Mordasini et al. (2015) following a piecewise approach based on the analytical treatments of Hahn & Malhotra (2005) and Walsh et al. (2011). The simulations assume that the protoplanet initially undergoes a damped Type I migration. During the growth of the planetary core from M_0 to the critical value M_C, the protoplanet proceeds through a linear regime of slow Type I migration that accounts for 40% of the total radial displacement of the giant planet. When the critical mass is reached and the runaway gas accretion phase begins,

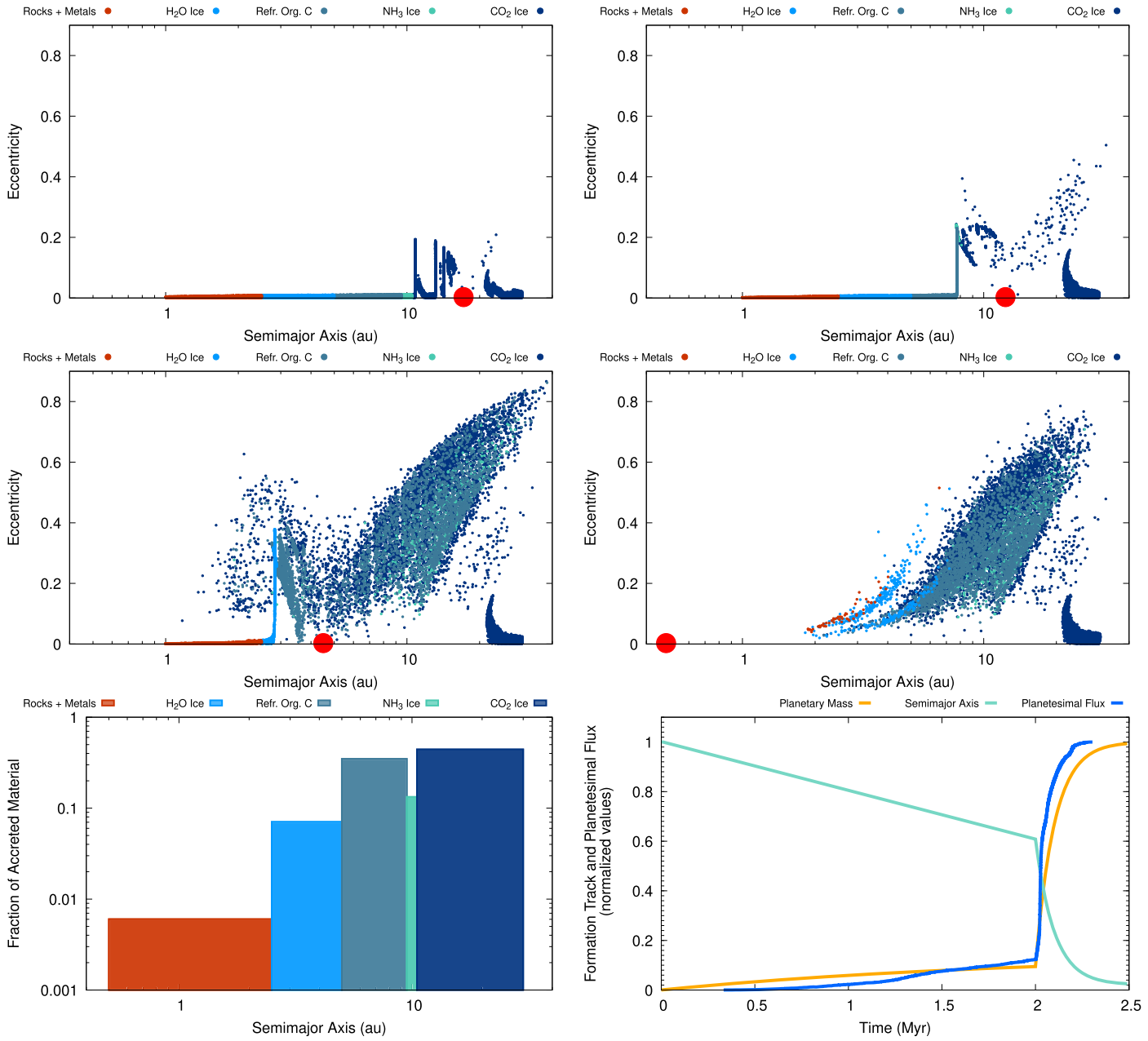

Figure 1. Snapshots of the *N*-body simulations performed with MERCURY-ARχES, describing the formation and migration of a giant planet in a dynamically evolving disk of gas and planetesimals. The four panels at the top and at the center of the figure show the dynamical evolution of the planetesimals in response to the growth and migration of a giant planet (large red circle) that starts forming at 19 au. From left to right and from top to bottom, the panels show the snapshots of the *N*-body simulations at 0.5, 1.8, 2.1, and 2.5 Myr. Different colors are used to distinguish planetesimals that formed beyond specific snowlines, as indicated in the legend. The two bottom panels are both snapshots taken at 2.5 Myr. The histogram on the left illustrates the fractions of solid material accreted from the different compositional regions of the disk. The plot on the right shows the tracks of the mass growth (orange curve) and the planetesimal accretion (blue curve) normalized to their final values. The green curve follows the evolution of the planet's semimajor axis normalized to its initial value.

(An animation of this figure is available.)

the protoplanet enters a faster regime of Type I migration. Once the protoplanet becomes massive enough to open a gap in the disk, it transitions to the slower Type II migration regime. These two last phases take the form of a power-law migration regime that accounts for the remaining 60% of the total radial displacement of the giant planet. The green curve in the bottom-right panel of Figure 1 shows an example of the migration track normalized to its initial value for the case of a giant planet that starts forming at 19 au.

The simulations model a total of six migration scenarios, with the protoplanet starting at 5, 12, 19, 50, 100, and 130 au from the star and ending at 0.4 au. The initial positions span the ranges of the observed architectures of giant planets in the solar system (5–10 au), in exoplanetary systems (from fractions of au to 20 au), and in circumstellar disks (100–150 au). The choice of a wide range of distances is meant to investigate the compositional implications of such diverse formation regions.

2.3. Ionization Environment of the Disk

As part of our exploration of the parameter space, we investigated how the final composition of the planet changes as

we vary the level of chemical activity in the disk. To this aim, we took advantage of the results by Eistrup et al. (2016), who modeled the ionization environment of the protoplanetary disk as set by two key sources. Specifically, they considered the ionization from the decay of short-lived radionuclides (SLRs) and from cosmic rays (CRs). For both disk chemical setups they analyzed (inheritance and reset, see Section 2.4), they explored a case of low ionization level, in which SLRs are the only source of ionization, and a case of high ionization level, in which an additional contribution from CRs of external origin is also taken into account. This results in a total of four disk chemical scenarios that we used to derive realistic planetary compositions from the outcomes of the simulations of Paper I. Future works will address the dependency of our results on a more detailed treatment of the interaction between the disk and the sources of ionization (Padovani et al. 2016, 2018; Rodgers-Lee et al. 2020).

In the low ionization scenario, the dominant contribution to ionization comes from the decay products of ^{26}Al, ^{36}Cl, and ^{60}Fe, which have half-lives $t_{\rm half}$ of 0.74, 0.30, and 2.6 Myr, respectively (Cleeves et al. 2014). Eistrup et al. (2016) adopted a simplified version of the analytical prescription given in Equation (30) by Cleeves et al. (2013b) for the ionization rate per H_2 molecule at the disk midplane:

$$\zeta_{\rm SLR}(r) = (1.25 \times 10^{-19}\,{\rm s}^{-1})\left(\frac{\Sigma(r)}{\rm g\ cm^{-2}}\right)^{0.27}, \quad (4)$$

where $\Sigma(r)$ is the surface density of the disk as a function of the radius r. Equation (4) does not account for the time decay of the ionization rate. Therefore, in the SLRs-dominated environment by Eistrup et al. (2016), the ionization rate is constant in time and higher in the inner and denser regions of the midplane.

For the high ionization scenario, in addition to SLRs, Eistrup et al. (2016) included a contribution of cosmic rays originating from outside the system. They parametrically modeled the CR ionization rate per H_2 molecule as:

$$\zeta_{\rm CR}(r) = (1 \times 10^{-17}\,{\rm s}^{-1}) \cdot \exp\left(\frac{-\Sigma(r)}{96\ {\rm g\ cm^{-2}}}\right), \quad (5)$$

where the characteristic value of $\zeta_{\rm CR} \sim 10^{-17}\,{\rm s}^{-1}$ is the interstellar rate that is typically assumed in models of disk chemistry (Webber 1998; Cleeves et al. 2014). The addition of CRs allows for higher ionization in the outer disk, where the surface density is lower and CRs can more efficiently penetrate into the midplane.

The aim of considering the two scenarios is to investigate the impact of ionization-driven chemical activity on the chemical composition of the disk midplane. Both the prescriptions given by Equations (4) and (5) should be interpreted as conservative estimates of the rates that regulate the ionization environment of a typical midplane. A recent study by Padovani et al. (2018) suggests that the CR ionization rate in high-density environments is higher than the typically assumed value of $10^{-17}\,{\rm s}^{-1}$. Moreover, the model by Eistrup et al. (2016) includes only attenuation due to the disk's surface density. Works by Cleeves et al. (2013a, 2013b, 2014) revealed that the CR flux at the disk's surface may be strongly attenuated by winds and/ or magnetic fields. In particular, modulation by stellar winds may reduce the CR flux reaching the midplane by many orders of magnitude ($\zeta_{\rm CR} \lesssim 10^{-20}\,{\rm s}^{-1}$), leaving SLRs as the dominant midplane ionization source (Cleeves et al. 2013a). Nevertheless, as mentioned before, the abundances of SLRs do evolve with time. As pointed out by Cleeves et al. (2013b), the SLRs ionization rate scales with the inverse of $t_{\rm half}$ and long-lived radionuclides (e.g., ^{40}K) only produce ionization rates of the order of $\sim 10^{-22}$ s^{-1} or even less. Moreover, although there is evidence of an enhanced abundance of SLRs in the early solar system, little is still known about their actual contribution to the total ionization rate in the midplane of a typical disk (Cleeves et al. 2013b).

Regarding other sources of ionization, Cleeves et al. (2013a) showed that photoionization from stellar and interstellar UV acts largely on C-bearing species in the upper atmosphere of the disk, leaving the midplane essentially unaffected. On the other hand, X-ray photons from the star penetrate deeper and dominate the intermediate layers of the disk. Only the scattered component of stellar X-rays is able to reach the midplane (Ercolano & Glassgold 2013). However, for a stellar X-ray luminosity of $L_X = 10^{29.5}$ erg s^{-1}, the scattered X-rays are expected to produce ionization rates falling in the range $\zeta_{\rm CR} \sim (1\text{–}10) \times 10^{-21}\,{\rm s}^{-1}$, far below the rates associated with SLRs and CRs, with minimal impact on the midplane chemistry (see Cleeves et al. 2014, and Figure 2 and 3 therein). Concerning X-ray background fields, as in the case of a protoplanetary disk embedded in a cluster, recent works revealed that these would have relatively little impact on disk chemistry (Meijerink et al. 2012; Rab et al. 2018). In particular, for an ordinary disk in a typical low-mass star-forming region, the ionization rate produced by an X-ray background flux of 2×10^{-4} erg cm^{-2} s^{-1} would equal the interstellar $\zeta_{\rm CR}$ only in the outer disk, at $r \sim 200$ au from the central star (see Rab et al. 2018, and Figure 10 therein).

2.4. Compositional Model of the Disk

To characterize the chemical environment in which the giant planet forms and migrates, we used an updated version of the compositional model presented in Paper I. The model quantifies the composition of the disk over its key components: rocks, organics, ices, and gas. In this work, we introduce a more realistic abundance profile for the refractory organic carbon, and we revise the treatment of the volatile component to allow for different evolutionary scenarios and ionization levels. Here, we outline the key features of the model, and we provide details on its refinements. We refer the reader to Paper I for a complete discussion.

We adopted the protosolar composition for both the star and its hosting protoplanetary disk. The protosolar elemental abundances, which characterize the original mixture of gas, were taken from Asplund et al. (2009) and Scott et al. (2015a, 2015b). Overall, they result in mass fractions $X = 0.7148$, $Y = 0.2711$, and $Z = 0.0141$, of H, He, and heavy elements, respectively. The gas composition sets the initial conditions for the condensation sequence across the disk, which regulates the distribution of the elements among the different phases (gas and solid) and carriers (rocks, organics, gas, and ices). As in Paper I, we focus on four tracing elements: C, O, N, and S. Their partitioning between the three solid components and between the solid and gas phases is derived from solar system data and recent results from astrochemical models, as discussed below.

2.4.1. Refractory Elements and Rocks

Based on meteoritic (Lodders 2010; Palme et al. 2014) and cometary (Le Roy et al. 2015; Altwegg et al. 2019; Rubin et al. 2019, 2020) data, we assumed that rock-forming elements are subtracted from the gas phase and locked into rocks in meteoritic proportion. In this framework, the comparison between meteoritic (Lodders 2010; Palme et al. 2014) and protosolar abundances (Asplund et al. 2009; Scott et al. 2015a, 2015b) reveals that rock-forming elements account for a mass fraction $Z_{\rm rock} = 6.67 \times 10^{-3}$ of the total gas in the disk. By subtracting the meteoritic abundances from the protosolar ones, we computed the initial abundances of the elements that remain in the gas phase as volatiles. Their partition across the different molecular carriers will be discussed in Section 2.4.2.

Focusing on the four elemental tracers considered in this work, the residual gas in our model contains 51% of the protosolar O and the majority of C (91%) and N (97%). The fact that almost half of the total O is trapped in rocks while N remains almost entirely in the gas phase, has important consequences for the final elemental ratios in giant planet atmospheres. One of them is that the N/O ratio of giant planets that derived most of their metallicity from the accretion of gas is always superstellar (see Section 3 for a more detailed discussion of this and other implications). While the gas remains substantially enriched in C, O, and N, the totality of S is trapped in solids as chondritic rocks across the whole disk. In this work, we assumed rocks to be fully incorporated into planetesimals at the onset of our simulations, which makes S particularly effective in tracing the planetesimal accretion (see Section 3.4 for further discussion).

2.4.2. Volatiles

The partition of volatiles across the different phases and carriers in the protoplanetary disk is based on the astrochemical models by Eistrup et al. (2016), who simulated four different scenarios obtained by varying the chemical initial conditions in the disk and the incident flux of ionizing radiation. Specifically, they explored two disk chemical scenarios called *inheritance* and *reset*. In the inheritance scenario, the disk is assumed to have inherited its initial composition from the original molecular cloud. Here, the initial conditions of the chemistry are set by the abundances of H, He, H_2, and eight key volatile molecules (see Eistrup et al. 2016, and Table 1 therein). In the reset scenario, the disk chemistry is instead completely reset due to heating from the protostar and the molecular gas of the disk, except for H_2, is fully dissociated into atoms. The chemical network is therefore evolved starting from atomic initial abundances of H, He, C, O, N, and S, plus molecules of H_2. Each of the two scenarios was analyzed under conditions of both low and high levels of ionization, as described in Section 2.3 and in Eistrup et al. (2016).

To model the distribution of C, O, and N across their molecular carriers in the four scenarios discussed above, we employed the radial abundance profiles by Eistrup et al. (2016) of the main volatile molecules in the gas and ice phases, produced by their full chemical network after 1 Myr of evolution. In doing so, we had to account for two major differences between our compositional model and the one by Eistrup et al. (2016). First, Eistrup et al. (2016) consider a disk with a single component of volatiles, which evolves in the gas phase and partly condenses into ices. As mentioned before in this section, our compositional model describes a three-component disk in which rocks and refractory organic carbon are formed alongside volatiles. Second, Eistrup et al. (2016) start from the total initial abundances of volatiles that are modeled over those of the interstellar medium. In our model, the three components originate from a mixture of gas with protosolar elemental abundances. We then performed a rescaling of the radial abundance profiles by Eistrup et al. (2016) to account for the additional components in the disk and to ensure that the protosolar abundances are retrieved throughout the disk for each tracing element.

To perform the scaling, we took advantage of the fact that chemical networks characterized by very different timescales can be treated independently of each other. Details of the adopted procedure are provided in the remainder of this section.

For the two inheritance scenarios, we followed the approach described in Paper I. Eistrup et al. (2016) report a total initial abundance of N (6.30×10^{-5}) smaller than that available to form volatiles in our model (7.22×10^{-5}). To ensure the conservation of the total mass of N, we then scaled up the total abundance of N and the abundance profiles of NH_3, and N_2 from Eistrup et al. (2016) by a factor of 1.15. When it comes to C and O, the two of them share a joint chemical network, which in turn requires using the same scaling factor for C- and O-bearing volatiles in order to preserve their relative proportions in the astrochemical model. We then scaled down the total abundances of both C and O and of their volatile molecular carriers by a factor of 0.53. The factor was computed by comparing the total initial abundance of volatile O (5.20×10^{-4}) reported by Eistrup et al. (2016) with the one available in our model to form volatiles (2.74×10^{-4}), which takes into account the fact that almost half of the protosolar oxygen is sequestered into rocks (see also Section 2.4.1). The remaining abundance of 1.9×10^{-4} of C (∼60% of the total protosolar abundance) is associated with refractory organic carbon (see also Paper I for further discussion), consistently with cometary and interstellar medium (ISM) data (Bergin et al.2015).

When considering the reset scenarios, two additional N-bearing species, HCN and NO, reach non-negligible abundances throughout the disk. However, both HCN and NO form more rapidly than NH_3 and N_2. Specifically, HCN and NO form quickly through gas phase reactions (Schwarz & Bergin 2014; Eistrup et al. 2016), alongside the other volatile C- and O-bearing molecules (e.g., CO and CO_2). On the other hand, the formation of NH_3 is governed by the slower gas–grain chemistry. The formation of N_2 occurs at an intermediate timescale. In the network of N, is therefore reasonable to assume that the formation of HCN and NO, and of NH_3 and N_2 proceeds through separate pathways. Specifically, the formation of HCN and NO occurs at early stages and is limited by the availability of atomic C and O in the gas phase. NH_3 and N_2 form later on from the residual N left by the previous reactions. When calibrating the radial abundance profiles, this translates into using different scaling factors for the formation pathways of HCN and NO, and of NH_3 and N_2. Specifically, we scaled the abundances of HCN and NO down by the same factor we applied to O- and C-bearing species, this factor being 0.53 as in the case of the inheritance scenarios. The excess of N at each location in the disk was then used to compute the scaling factor of N_2 and NH_3. As in the inheritance, also in the reset

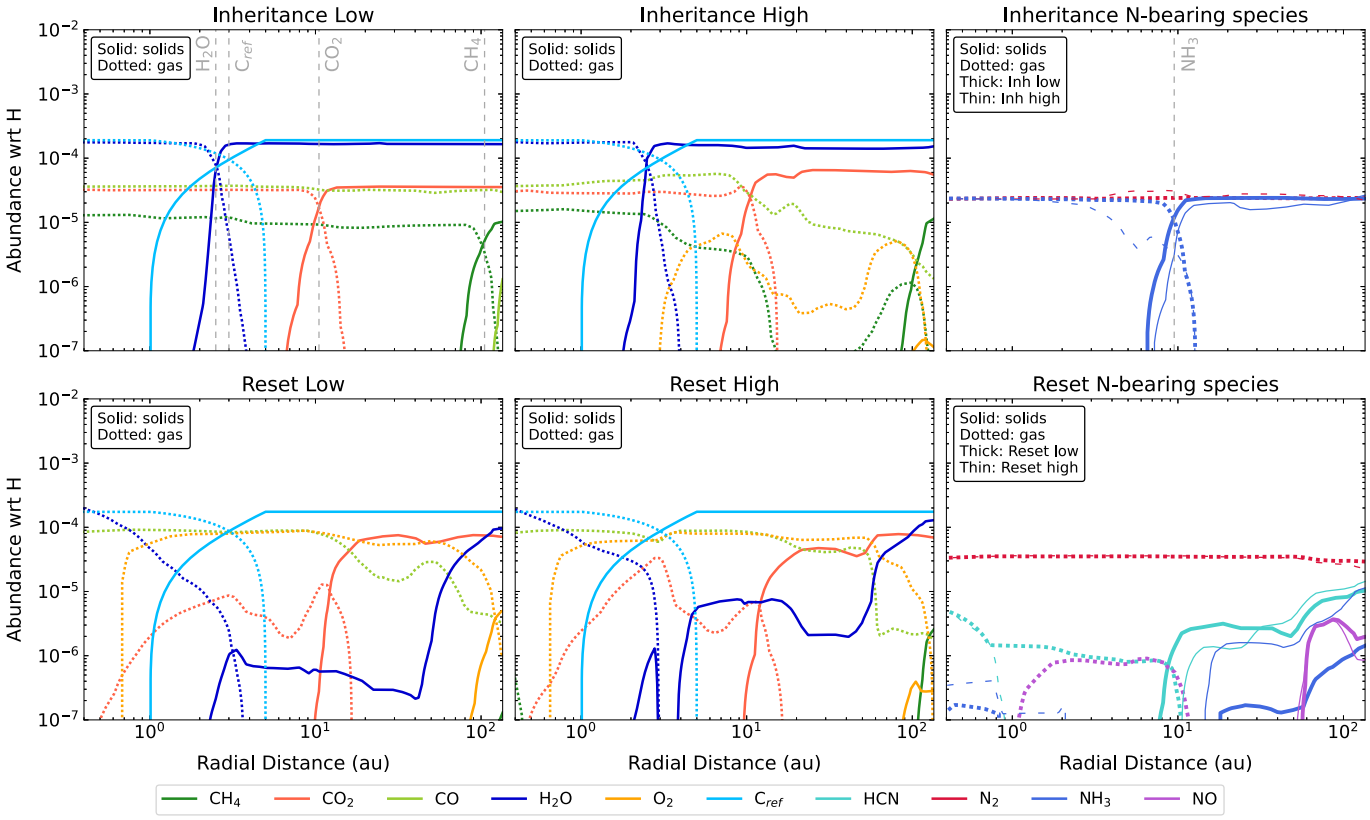

Figure 2. Radial profiles of molecular abundances of the key volatile C-, O-, and N-bearing species with respect to total H atoms. The profiles are taken from Eistrup et al. (2016) and properly rescaled to account for the different disks and the different compositional models considered in this work. In all panels, solid and dotted lines indicate the solid and gas phases, respectively. The top three panels describe the two inheritance scenarios, while the bottom three ones describe the two reset scenarios. The left-hand and central panels show the abundances of the key volatile molecules carrying C and O, including the contribution of refractory organic carbon (C_{ref}). N-bearing molecules are shown in the two right-hand panels for visual ease. Here, the low (SLRs only) and high (SLRs and CRs) ionization levels are shown in the same plot by means of thick and thin lines, respectively. The gray, dashed, vertical lines in the plots of the inheritance low scenario indicate the position of the snowlines of H_2O (2.5 au), C_{ref} (3 au), NH_3 (9.4 au), CO_2 (10.5 au), and CH_4 (105 au). CO and N_2 condense beyond 130 au in our model, and their snowlines are therefore not seen. Snowlines are omitted in the other scenarios, as the complexity of the chemistry requires the introduction of multiple snowlines.

scenarios, a fraction of atomic C is associated with refractory organic carbon. In this case, the total abundance is 1.7×10^{-4}. The rescaled molecular abundance profiles used in this work are plotted in Figure 2 for both the inheritance and the reset scenarios.

The most noticeable effect of varying the level of chemical activity is that the snowlines become less unequivocally defined, as multiple snowlines for the same molecule can exist at different locations in the disk. The O_2 carries a significant fraction of O across all scenarios, except for the inheritance low scenario, where the abundance of O_2 drops below 10^{-7}. Among the C-bearing species, the dominant contribution comes from organic compounds, whose origin is discussed in more detail in Section 2.4.3. The N_2 is the main carrier of N in all scenarios. As its snowline is located beyond 130 au for the adopted disk thermal profile, a large fraction of N remains in the gas phase across most of the disk. The fraction of N that condenses as ice is carried by NH_3 in the inheritance scenarios and by NH_3, HCN, and NO in the reset ones.

The focus of our compositional model is on the distribution of the four tracing elements, C, O, N, and S, across the gas and solid phases in the disk, not on the distribution of their respective molecular carriers, as represented by the radial abundance profiles. When it comes to volatiles, the relevant quantity to consider is therefore the abundance of each tracing element, computed as the sum of the abundances of all the molecular carriers of that specific element. The partition of the molecular abundance profiles in Figure 2 among C, O, N, and S, is shown in Figure 3 for both the inheritance and the reset scenarios. The dashed lines indicate the contribution from the gas phase, while the solid lines indicate that of solids. Note that the solid phase includes also the contribution from the rocks (see Section 2.4.1), in addition to the ices and the organics. The elemental abundances are normalized to their respective stellar value, indicated by the black, dashed, horizontal line. We adopt the superscript $*$ in the notation as a general convention to distinguish the normalized abundances from the absolute ones. In this scale, S is at the stellar level throughout the disk, being entirely locked into rocks. For the other elements, the trends reflect the phase changes of the disk material across the multiple snowlines. The major differences among the four scenarios are in the gaseous O, which shows higher abundances in the reset scenarios with respect to the inheritance ones. Such differences have a significant impact on the planetary elemental ratios that are computed from O. For instance, for planets that derived their metallicity from the accretion of gas in the reset scenarios, the large fraction of O locked in the gas phase translates into substellar C/O ratios. See Section 3.3 for further discussion of this and other effects.

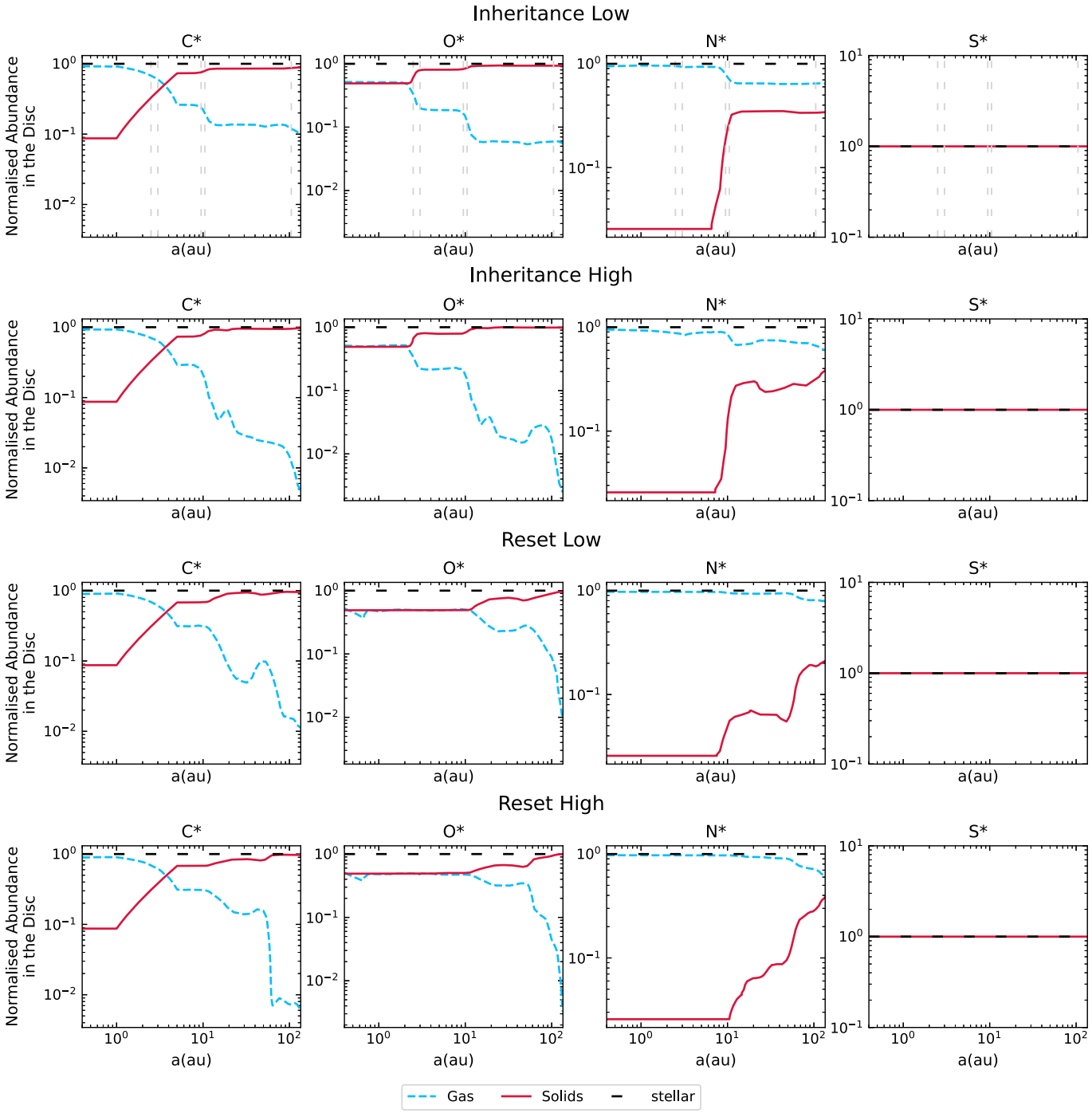

Figure 3. Elemental abundances of C, O, N, and S in the disk, normalized to their respective stellar value, for the gas (dashed lines) and the solid (solid lines) phases (the latter includes rocks, organics, and ices). The trends are extracted from the radial profiles of molecular abundances in the four chemical scenarios. The gray, dashed, vertical lines in the top four panels indicate, from left to right, the locations of the snowlines of H_2O (2.5 au), refractory organic carbon (3 au), NH_3 (9.4 au), CO_2 (10.5 au), and CH_4 (105 au). Such snowlines are unequivocally defined only in the inheritance scenario with a low ionization level, and for that reason they are omitted in the other scenarios. The black, dashed, horizontal line at 1 indicates the reference stellar value in all plots.

2.4.3. *Refractory Organics*

Following Cridland et al. (2019) and previous authors (e.g., Thiabaud et al. 2014; Bergin et al. 2015; Mordasini et al. 2016), our model includes a refractory C-bearing component as suggested by the comparison between the carbon deficit observed in the Earth (Allègre et al. 2001) and in solar system meteorites (Wasson & Kallemeyn 1988; Bergin et al. 2015) with respect to the ISM and comets (Bergin et al. 2015 and references therein; Bardyn et al. 2017). Such component accounts for ∼60% of the ISM carbon, yet it is unclear whether C is in the form of graphite, amorphous carbon grains, or organics. We adopted the terminology by Thiabaud et al. (2014) and Isnard et al. (2019), and we refer to this C reservoir as refractory organic carbon.

For the bulk composition of the inner solar system to be markedly carbon poor, refractory organic carbon needs to be destroyed in the inner Solar Nebula. In particular, following Lee et al. (2010), we assumed that it is completely destroyed

and released into the gas phase within 5 au. Following Mordasini et al. (2016) and Cridland et al. (2019), we introduced a snowline for refractory organic carbon with 50% condensation at 3 au, in both the inheritance and reset scenarios. The resulting abundance profile for the condensed phase is zero inside 1 au, then increases linearly up to 5 au, where it reaches the value of 1.9×10^{-4} in the inheritance scenario and of 1.7×10^{-4} in the reset one (see Section 2.4.2), and remains constant thereafter. The distribution of refractory organic carbon across the disk is shown Figure 2 by means of light-blue curves.

3. Results and Discussion

As introduced in Section 2, in order to explore the implications of the disk chemistry for the chemical composition of the planetary atmospheres, we coupled the outcome of the *N*-body simulations from Paper I with the four compositional models of the disk. The simulations describe a planetary embryo that starts its growth and migration in different compositional regions of the disk, specifically migrating from 5, 12, 19, 50, 100, and 130 au to 0.4 au (see also Figure 1). Each simulation traces the accreted masses of both gas and planetesimals at each location along the migration pathway.

For each simulation and compositional model we proceeded as follows. We first used the radial abundance profiles of the main molecular carriers of C, O, N, and S (Figure 2) and the relevant atomic weights to extract the individual mass contributions of the four tracing elements from the accreted masses of gas and solids. Under the assumption of homogeneous mixing in the planetary envelope (see Paper I for discussion), for each element we computed the total accreted masses of gas and solids along the formation pathway. We then converted such masses into total abundances with respect to H atoms. The results were used to compute the elemental ratios C/O, C/N, N/O, and S/N, in the final atmosphere of the planet, for both the gas and solid phases. As discussed in Paper I, when considering both contributions from the accreted gas and solids, the giant planet is *solid enriched*. In this case, the planet envelope is characterized by superstellar abundances of most if not all the elements. On the other hand, when considering only the accretion of gas, the giant planet is *gas dominated*. For the adopted compositional model of the disk, gas-dominated giant planets are characterized by substellar abundances (see Paper I and Turrini et al. 2022 for further discussion of alternative scenarios).

The final step in our analysis was to compute the atmospheric elemental ratios normalized to their stellar counterparts. In this scale, values of the ratios equal to 1 are reflective of a giant planet whose chemical composition matches that of its host star. In this sense, normalization provides a tool to measure the deviation of the planet's composition from the stellar one. The results can then be generalized to systems in which the composition of the host star differs from the solar one considered in this work. To differentiate between absolute and normalized ratios, we refer to the latter as C/O^*, C/N^*, N/O^*, and S/N^*.

The results of our analysis are plotted for each of the four scenarios in Figures 4, 5, 6, and 7, while their trends for each elemental ratio are compared in Figure 8. The results reveal that the joint use of different elemental ratios proves to be the key to accurately characterize the formation of giant planets in terms of:

1. the accretion history, i.e., whether it was dominated by the gas or the planetesimals,
2. the extent of the migration,
3. the chemical initial conditions of the protoplanetary disk (only for gas-dominated giant planets).

We will delve into each of these aspects in Sections 3.3, 3.4, and 3.5. Before doing that, however, it is worth discussing some important concepts to have in mind when interpreting the information in Figures 4, 5, 6, and 7.

3.1. Linking Planetary Atmospheres to Disk Structures

The final composition of giant planets is generally expected to reflect the chemical structure of the protoplanetary disk, especially that of the region of the disk where the planet was born (e.g., Öberg et al. 2011; Lothringer et al. 2021). We can assess the degree to which this assumption is reasonable by comparing the elemental ratios in the two environments. The results of such analysis are illustrated in Figures 4–7. Each figure examines one of the four chemical scenarios. The top two panels show the normalized elemental ratios in the atmosphere of gas-dominated (on the left) and solid-enriched (on the right) giant planets at the end of the six simulations. The lines connecting the different scenarios are provided as a visual aid only. The bottom four panels show the radial profiles of the normalized elemental ratios in the disk, as computed from Figure 3. Such profiles can be seen as snapshots of the midplane chemical structure, where solid and dashed lines characterize the solid and gas phase, respectively.

Overall, the four figures show that the atmosphere of the giant planet inherits only part of the chemical properties of the disk. Specifically, elemental ratios that are sub- or superstellar in the disk will generally be so in the planet as well. However, the results also show that this disk-planet link cannot be used to make quantitative predictions. Specifically, the plots reveal that for some migration scenarios the normalized elemental ratios in the planet and in the disk do not immediately relate. For instance, although the S/N^* is markedly superstellar throughout the disk and increases toward the star, its value in the solid-enriched giant planet that starts forming at 5 au drops to the substellar level. The final composition of the planet envelope depends crucially on how efficiently the gas and the solids are accreted from each region of the disk along the migration pathway. For gas-dominated giant planets, the accretion of gas reaches its maximum during the runaway gas accretion phase (see Section 2.2). The final atmosphere of the planet will therefore be strongly influenced by the chemical properties of the region of the disk traversed by the planet during this phase. In solid-enriched giant planets the accretion of gas and solids are coupled, but their relative contribution to the planetary metallicity depends on the extent of the migration. In particular, the larger the migration the larger the number of planetesimals encountered by the planet and the larger the contribution of planetesimal accretion to the final metallicity. As the planet migrates for shorter distances, it encounters and accretes fewer planetesimals, and the contributions to its metallicity by gas and solids become comparable. As a consequence, the elemental ratios of solid-enriched giant planets follow the global trends of the disk solid component only in large-scale migration scenarios, while diverging from them for limited migrations.

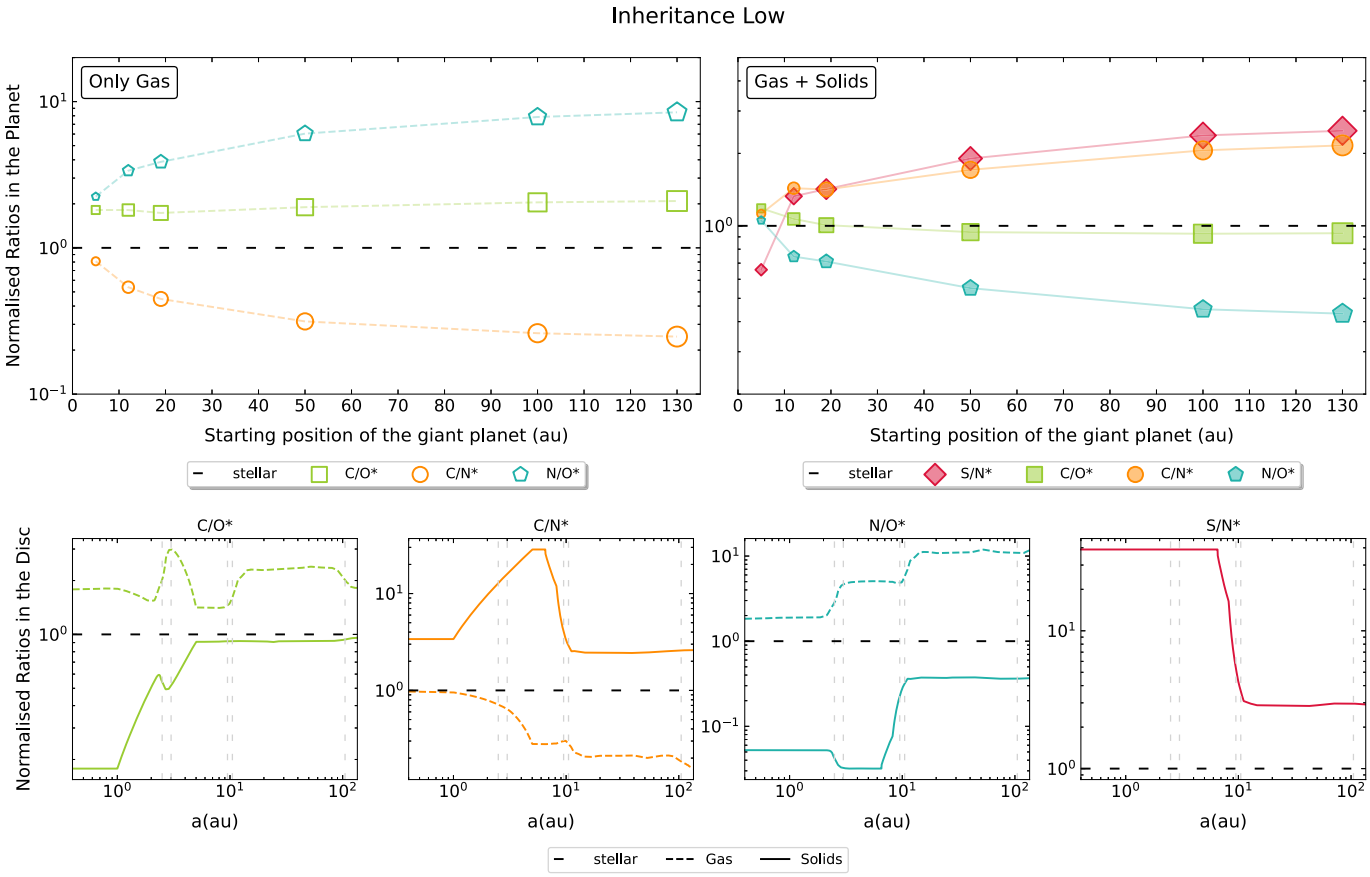

Figure 4. Normalized elemental ratios in the final atmosphere of the planet (top two panels) and in the disk (bottom four panels) in the inheritance scenario with low ionization. The top two panels show results for the six migration scenarios, corresponding to initial semimajor axes of 5, 12, 19, 50, 100, and 130 au. The increasing size of the markers maps the increasing distance traveled by the planet in the six migration scenarios. Linking lines are shown only for visual ease. The plot on the left (with empty markers) describes a gas-dominated giant planet, while the plot on the right (filled markers) is for solid-enriched ones. The bottom four panels show the trends of the elemental ratios on the disk for the gas (dashed lines) and the solid (solid lines) phases. The gray, dashed, vertical lines, from left to right, indicate the position of the snowlines of H_2O (2.5 au), refractory organic carbon (3 au), NH_3 (9.4 au), CO_2 (10.5 au), and CH_4 (105 au). The black, dashed, horizontal line at 1 indicates the reference stellar value in all plots.

The decreasing trend of the planetary S/N^* ratio from large- to short-scale migrations can be easily understood considering how S and N are distributed in the disk and how they are accreted on the planet. In our disk, S is entirely locked in the solid phase, while N is almost entirely in the gas phase as N_2, slightly deviating from the stellar value beyond the NH_3 snowline (see Figure 3). As a direct consequence of this partitioning, in the planet envelope the total S scales linearly with the accreted planetesimals, while the total N is accreted in stellar proportion almost independently on the radial migration. Consequently, even though the S/N^* ratio of solids in the inner disk is about 40 times higher than the stellar value, for short-scale migrations the contribution of the accreted N becomes large enough to bring the S/N^* ratio in the planet to substellar value. Similar arguments can be used to explain why the N/O^*, C/O^*, and C/N^* ratios of solid-enriched giant planets approach stellar values for short-scale migrations.

Our results emphasize how the composition of giant planets and their atmospheres can be connected to that of their native disks only by coupling the disk chemical structure with the growth and migration tracks that characterize planet formation. With this in mind, we can proceed with the discussion of our results and their implications for planet formation.

3.2. The Diagnostic Power of the C/O Ratio

Figure 8 compares the normalized elemental ratios of solid- and gas-dominated giant planets in the inheritance (blue points) and reset (red points) scenarios. The results are shown for each of the six simulations, identified by the location of the planet at the onset of its formation. The C/O^* ratio shows almost flat trends, revealing a rather limited diagnostic power.

For short-scale migrations, the C/O^* ratios in all scenarios vary between 1 and 2 times the stellar value. The limited variations between the different disk chemistry and planet migration scenarios are too small to be unequivocally resolved with the current accuracy of retrieval methods, which is of the order of 20% (see Barstow et al. 2020 and Paper I for further discussion). Therefore, giant planets that formed close to the star in a disk that inherited its composition from the prestellar core cannot be observationally distinguished from those that formed in a disk that experienced a complete reset of the chemistry, nor can we resolve whether they are gas dominated or solid enriched.

The degeneracy is partially broken for large-scale migrations, where the C/O^* ratio of solid-enriched and gas-dominated giant planets follows distinct trends. Specifically, solid-enriched giant planets are characterized by stellar values of the C/O^* ratio, independent of how far the planet started its migration and the chemical structure of the birth environment.

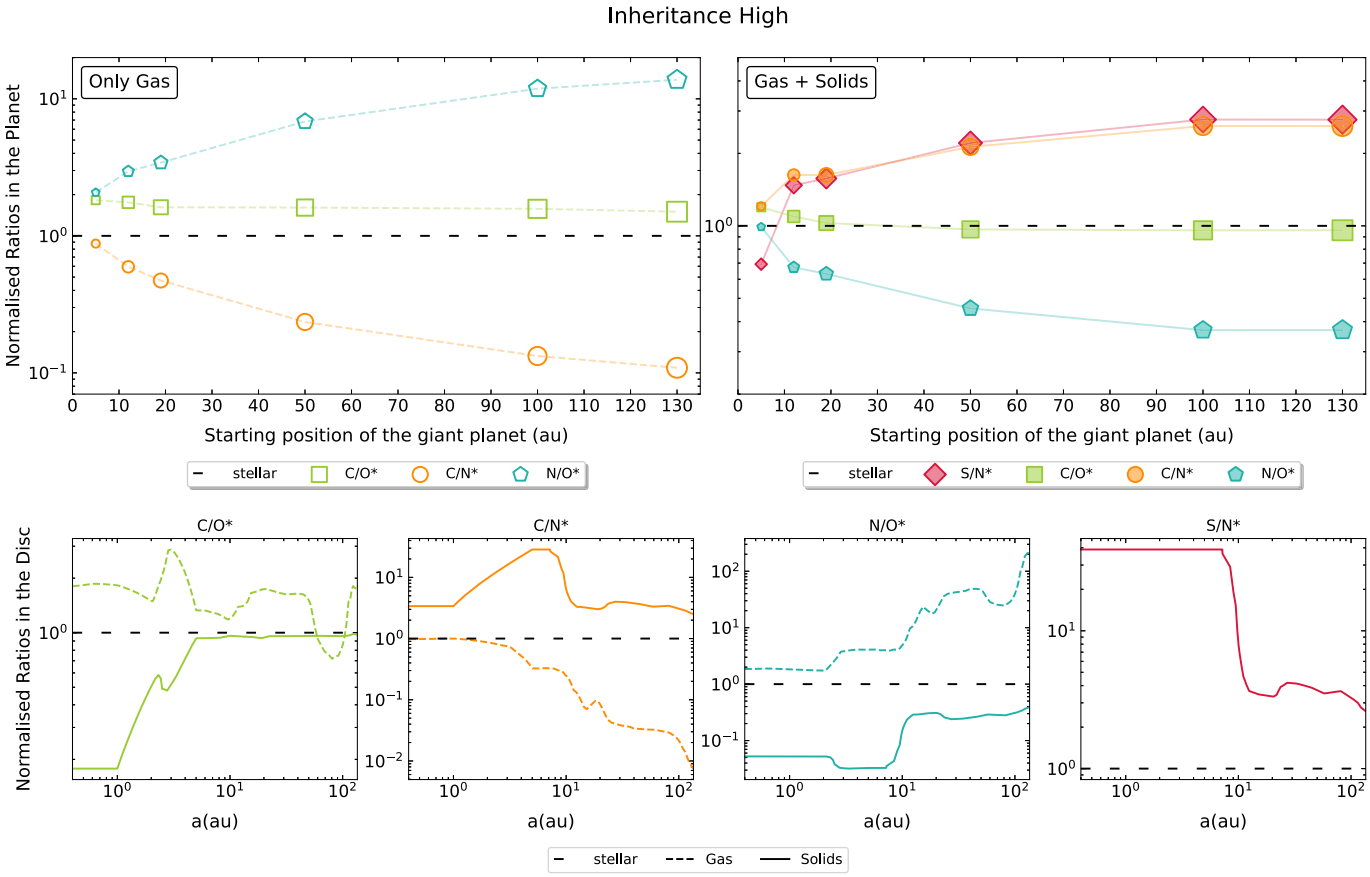

Figure 5. Normalized elemental ratios in the final atmosphere of the planet (top two panels) and in the disk (bottom two panels) in the inheritance scenario with high ionization. The top two panels show results for the six migration scenarios, corresponding to initial semimajor axes of 5, 12, 19, 50, 100, and 130 au. The increasing size of the markers maps the increasing distance traveled by the planet in the six migration scenarios. Linking lines are shown only for visual ease. The plot on the left (with empty markers) describes a gas-dominated giant planet, while the plot on the right (filled markers) is for solid-enriched ones. The bottom four panels show the trends of the elemental ratios on the disk for the gas (dashed lines) and the solid (solid lines) phases. The black, dashed, horizontal line at 1 indicates the reference stellar value in all plots.

On the contrary, gas-dominated giant planets are characterized by a C/O^* ratio significantly deviating from the stellar value. In this case, the C/O^* ratio provides constraints on both the migration and the disk chemical scenario. Detailed discussion on each of these individual aspects is provided in Sections 3.3, 3.4, and 3.5.

3.3. Constraints on the Accretion History

As anticipated in Section 3.2, the C/O^* ratio provides information on the accretion history of giant planets only for large-scale migration scenarios. In this case, stellar values are associated with solid-enriched giant planets, whereas marked sub- and superstellar values provide an indication of accretion dominated by gas. Specifically, substellar C/O^* ratios are associated with gas-dominated giant planets in the reset scenarios, whereas superstellar values characterize gas-dominated giant planets in the inheritance scenarios.

To understand the origin of such trends we refer to the disk composition, as described by the molecular abundance profiles in Figure 2. Beyond 10 au, the gas phase in the reset scenarios is characterized by a lower abundance of CH_4 and higher abundances of CO and O_2 with respect to the inheritance scenarios. Because both CO and O_2 typically condense at very low temperatures, they act as reservoirs of gaseous O in most of the disk extension. Consequently, the abundance of total O^* in the gas phase is higher in the reset scenarios than in the inheritance ones. In particular, beyond 10 au, the abundance of O^* exceeds that of C^*. Such behavior is shown in Figure 3 and is the reason why the C/O^* ratio of the disk gas phase drops below the stellar value in the reset scenarios (see Figures 6 and 7). As higher abundances in the gas correspond to lower abundances in the solids, the opposite trend is observed for the C/O^* ratios of the disk solid phase. Moving from the disk to the planet, we recall that the final elemental ratios in the planet envelope depend on the mass accretion rate (see the discussion in Section 3.1). Such rate is a nonlinear function of the orbital distance, and it is highly influenced by the position on the disk where the runaway gas accretion occurs. As discussed in Section 2.2, in our model the runaway gas accretion phase begins once the first 40% of the total radial displacement of the planet has been covered. For migrations starting beyond 20 au, in our simulations, this means that the region traversed by the planet during the runaway gas accretion phase falls between 10 au and 80 au. Therefore, gas-dominated giant planets in the reset scenarios accrete most of their gas from the disk region in which the C/O^* ratio is substellar, which is why their final C/O^* ratio is also substellar. When it comes to solid-enriched giant planets, the contribution of planetesimal accretion to the envelope metallicity increases with the extent of migration. For large-scale migrations, the metallicity is dominated by the planetesimals accreted from the disk region in which the C/O^*

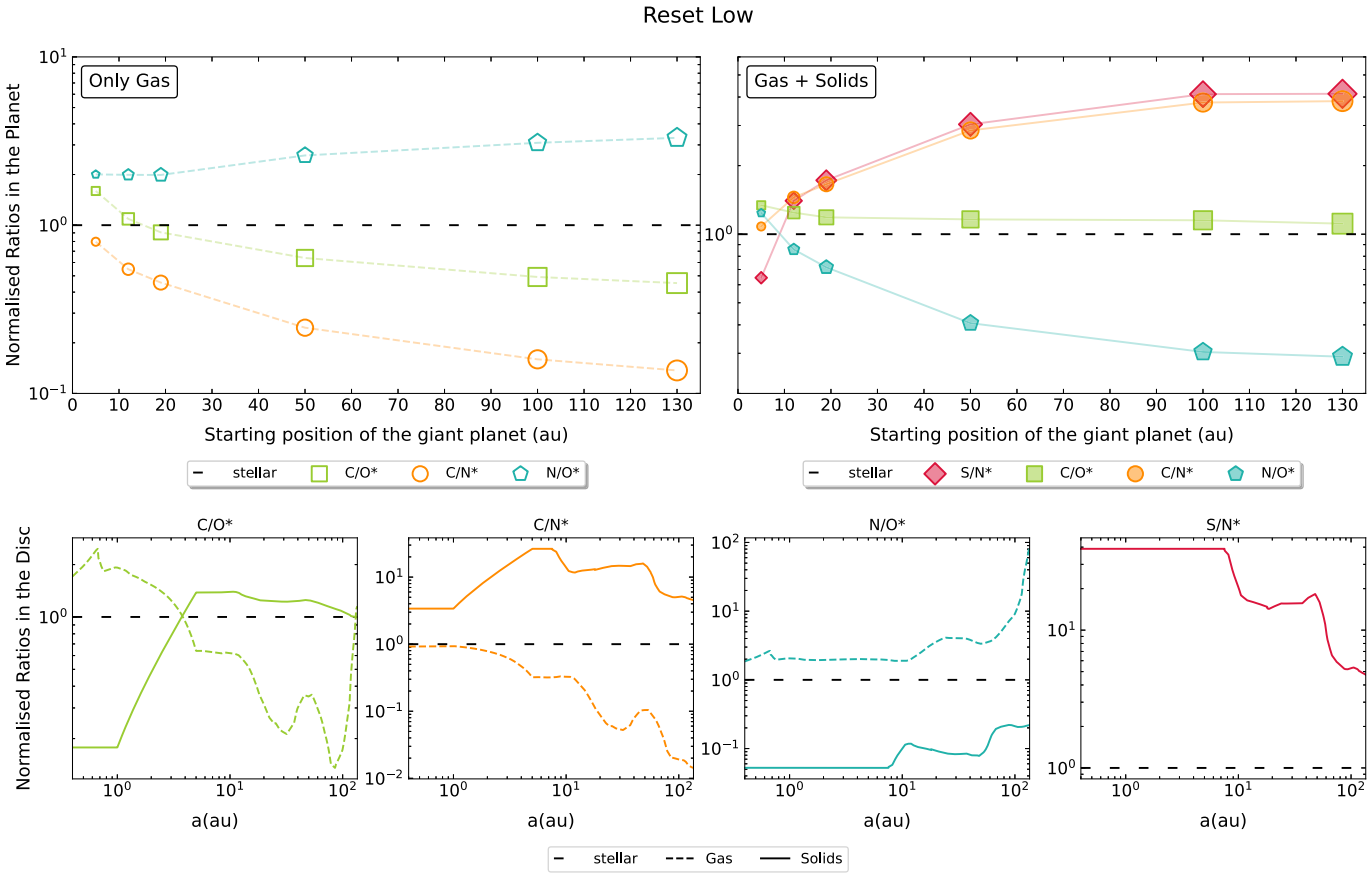

Figure 6. Normalized elemental ratios in the final atmosphere of the planet (top two panels) and in the disk (bottom four panels) in the reset scenario with low ionization. The top two panels show results for the six migration scenarios, corresponding to initial semimajor axes of 5, 12, 19, 50, 100, and 130 au. The increasing size of the markers maps the increasing distance traveled by the planet in the six migration scenarios. Linking lines are shown only for visual ease. The plot on the left (with empty markers) describes a gas-dominated giant planet, while the plot on the right (filled markers) is for solid-enriched ones. The bottom four panels show the trends of the elemental ratios on the disk for the gas (dashed lines) and the solid (solid lines) phases. The black, dashed, horizontal line at 1 indicates the reference stellar value in all plots.

ratio of the solids is superstellar, which is why the final C/O^* ratio in the planet envelope is also superstellar.

We highlight that in the inheritance scenario with a high ionization level, the C/O^* ratio of gas-dominated giant planets slightly decreases with increasing length of migration. For the accuracy of the current retrieval methods (see Section 3.2), this introduces a degeneracy of the planet's accretion history. Specifically, for very large-scale migration scenarios, gas-dominated giant planets in the inheritance high scenario would be indistinguishable from solid-enriched ones. Such a decreasing trend in the inheritance high scenario originates from the enhanced abundance of O^* between 50 au and 100 au in our disk model (see Figure 3), which in turn results from the peak abundance of O_2 in the outer disk (see Figure 2). In this region, the abundance of O^* exceeds that of C^*, hence bringing the disk C/O^* ratio to substellar values (see Figure 5). Gas-dominated giant planets that accrete most of their gas from this region will therefore be characterized by lower C/O^* ratios than in the inheritance low scenario.

The information provided by the C/O^* ratio on the planet accretion history can find independent confirmation in the total metallicity of the planet envelope. Gas-dominated giant planets are characterized by substellar envelope metallicities that decrease with migration, as highlighted also in Paper I. Solid-enriched giant planets are instead characterized by the opposite trend, i.e., superstellar envelope metallicities that increase with migration. Note that here the relevant quantity is the planetary metallicity normalized to that of the host star. The choice of the right stellar reference value is therefore key to the correct interpretation of observational data. The C/O ratio and metallicity of the Sun are widely used, either explicitly or implicitly, as referenced in interpreting the composition of exoplanetary atmospheres (see, e.g., Madhusudhan 2019 for a recent review). However, both the C/O ratio and the metallicity of stars in planetary systems can significantly deviate from their respective values in the Sun (e.g., Delgado Mena et al. 2010; Mulders 2018 and references therein; Magrini et al. 2022). Therefore, to avoid introducing biases, one has to look at the planetary elemental ratios and metallicity in the reference frame of the host star. For instance, a planetary C/O ratio estimated to be 0.55 (equal to the solar C/O ratio) would be stellar only if the planet formed around a solar-type star. If, instead, the planet formed around a star characterized by a subsolar C/O ratio (e.g., 0.45), the planetary C/O ratio should be correctly interpreted as superstellar. Our methodology has been recently successfully applied by Carleo et al. (2022) and Guilluy et al. (2022) to the interpretation of observational data from the GAPS 2 program.

It is important to notice that when the C/O^* ratio can only be estimated as being either sub- or superstellar, it is not possible to constrain the planet's accretion history, unless independent measurements of the envelope metallicity are available.

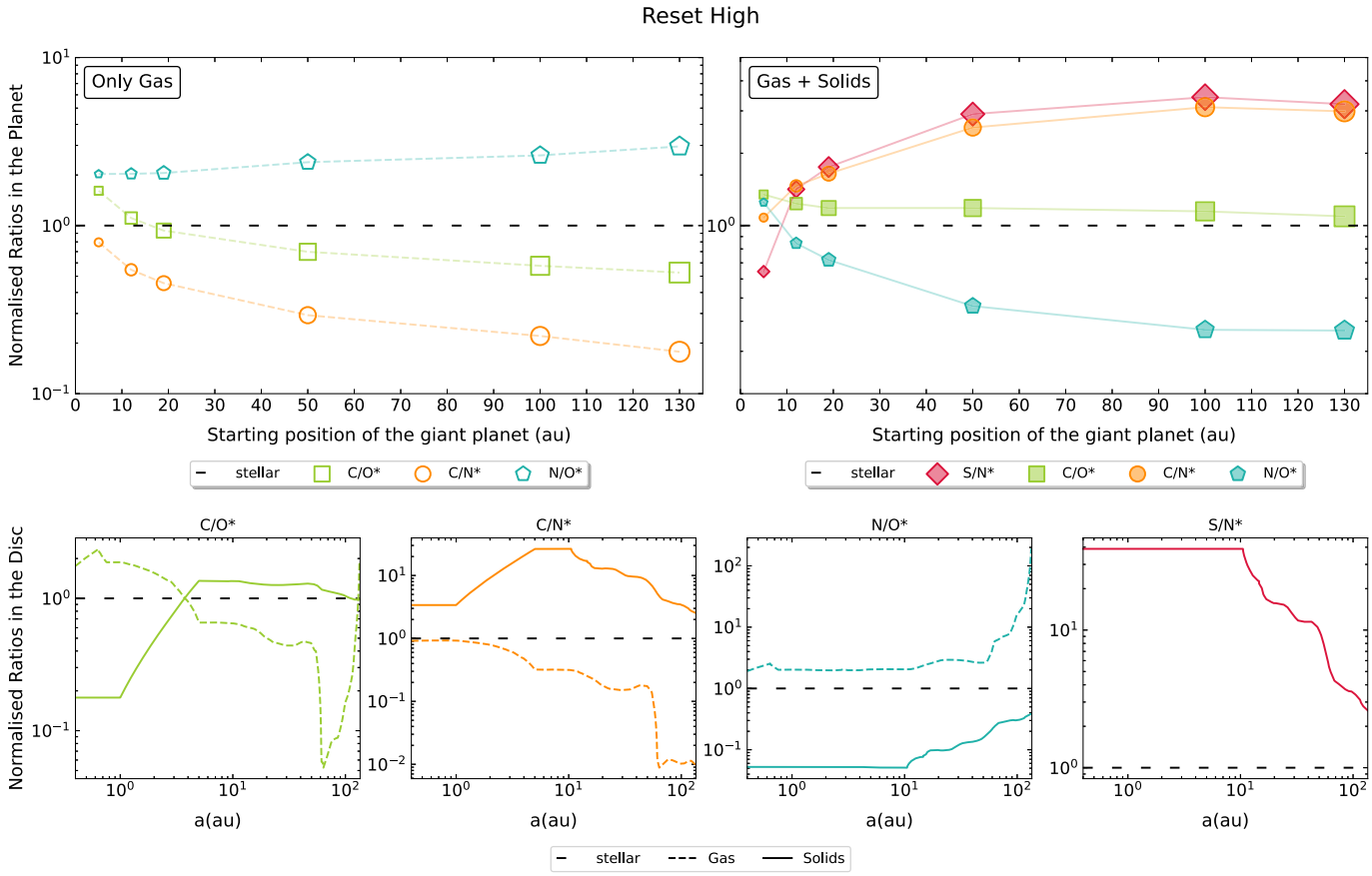

Figure 7. Normalized elemental ratios in the final atmosphere of the planet (top two panels) and in the disk (bottom four panels) in the reset scenario with high ionization. The top two panels show results for the six migration scenarios, corresponding to initial semimajor axes of 5, 12, 19, 50, 100, and 130 au. The increasing size of the markers maps the increasing distance traveled by the planet in the six migration scenarios. Linking lines are shown only for visual ease. The plot on the left (with empty markers) describes a gas-dominated giant planet, while the plot on the right (filled markers) is for solid-enriched ones. The bottom four panels show the trends of the elemental ratios on the disk for the gas (dashed lines) and the solid (solid lines) phases. The black, dashed, horizontal line at 1 indicates the reference stellar value in all plots.

Our findings reveal that using the C/O^* ratio alone to probe the formation pathways of giant planets could lead to wrong conclusions. The limited diagnostic power of the C/O^* ratio is essentially due to the high volatility of both C and O, which makes the ratio unable to unequivocally trace the accretion of gas and solids. The inclusion of N, one of the most volatile elements, in the set of elemental tracers allows the computing of the C/N^* and N/O^* ratios and the breaking of the degeneracy on the accretion history. Specifically, Figure 8 shows that for both the C/N^* and N/O^* ratios, the trends for gas-dominated and solid-enriched giant planets are well separated and always characterized by opposite behaviors. Such behaviors result from the lower volatility of C and O with respect to N. Specifically, while the bulk of N in disks remains in the gas phase as N_2, the abundances of gaseous C and O decrease toward the outer disk (see Figure 3). Variations of the C/N^* and N/O^* ratios in disks are therefore driven by variations of C^* and O^*. As a consequence, the C/N^* (N/O^*) ratio of gas-dominated giant planets is globally substellar (superstellar) and decreases (increases) with the radial migration. The behavior of solid-enriched giant planets is the opposite, with C/N^* (N/O^*) globally superstellar (substellar) and increasing (decreasing) with migration.

It is worth noticing that the N/O^* ratio of gas-dominated giant planets is always markedly superstellar and never drops below 2. Such a trend is due to the fact that in our model about 50% of O is early sequestered into rocks, hence subtracted from the gas phase. As a consequence, in short-scale migration scenarios, even if the other elemental ratios approach the stellar value, the N/O^* ratio does not.

What emerges from our study is that in order to get a complete picture of planet formation, one has to look at multiple elemental ratios. One of the advantages of using normalized ratios is that their trends can be more readily and intuitively compared. The comparison of the top two panels in Figures 4–7 reveals the existence of fixed relations between the ratios of gas-dominated and solid-enriched giant planets. In particular, regardless of the chemical scenario, the N/O^* ratio of gas-dominated giant planets is always larger than the C/O^* ratio, which is in turn larger than the C/N^* ratio. The opposite relation holds for solid-enriched giant planets for moderate and large-scale migrations. Such relations result from the differences in relative volatility between C, O, and N. More volatile elements are characterized by lower condensation temperatures. As such, they condense in solid form farther away from the star and remain in gas form over wider disk regions. As discussed in Section 2.4, in our compositional model, N is almost entirely present in the gas phase as N_2 in all four scenarios. Therefore, as a result of its high volatility, N will be proportionally more abundant than C and O in giant planets that accreted only gas, hence leading to $N/O^* > C/O^* > C/N^*$. For solid-enriched planets, which accreted from the solid phase that is

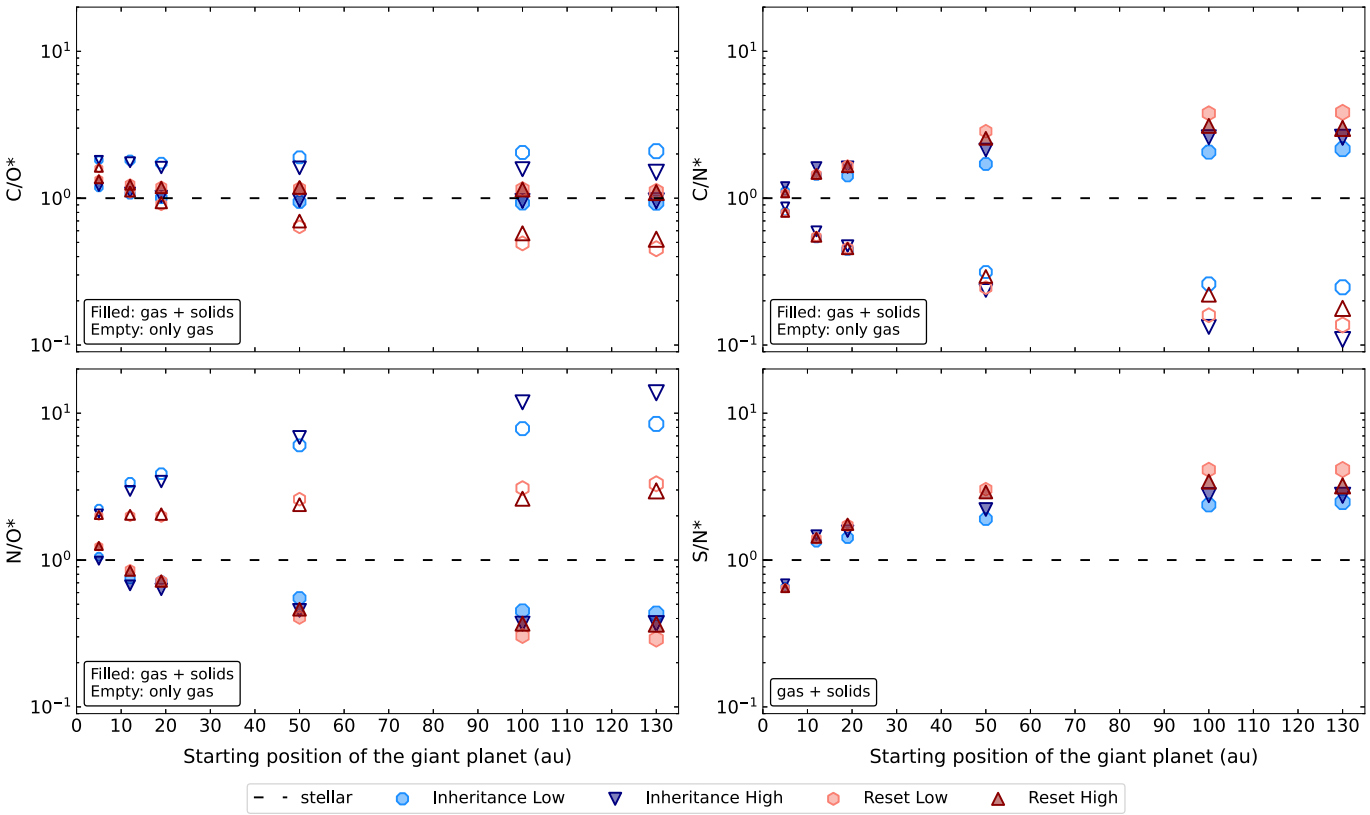

Figure 8. Elemental ratios C/O^*, C/N^*, N/O^*, and S/N^* normalized to their respective stellar value in the four chemical scenarios. The data are the same as in the top two panels of Figures 4–7, here being plotted together to be more easily compared with each other. The blue points refer to the inheritance scenarios, while the red ones refer to the reset scenarios. Specifically, the light-blue octagons and the light-red hexagons indicate low ionization level, while the dark-blue, downward triangles and the dark-red, upward triangles indicate high ionization level. The results are plotted for the six migration scenarios, corresponding to initial semimajor axes of 5, 12, 19, 50, 100, and 130 au. The increasing size of the markers maps the increasing distance traveled by the planet in the six migration scenarios. Trends for both the accretion scenarios are shown: filled markers for solid-enriched and empty markers for gas-dominated giant planets. The black, dashed, horizontal line at 1 indicates the reference value for giant planets whose chemical composition matches that of their host star.

progressively depleted in highly volatile elements, the opposite is true, and $C/N^* > C/O^* > N/O^*$. The emerging picture is that a joint evaluation of normalized elemental ratios allows us to immediately and unequivocally discriminate between planets that derive their metallicity from the accretion of gas and planets that experienced planetesimal enrichment. These results expand those of Paper I, showing how the relative values of the normalized ratios follow the same patterns independently on the underlying chemical scenario. These behaviors have been recently confirmed in the studies of Biazzo et al. (2022), Carleo et al. (2022), and Guilluy et al. (2022), based on Paper I.

3.4. How Far Did the Planet Start Its Migration?

Among all the ratios, C/O^* appears to be the least robust as a diagnostic tool for the migration history of the planet. In particular, Figure 8 shows that the C/O^* ratio exhibits limited changes among the migration pathways in almost all chemical scenarios. Its overall flatness is essentially due to the limited range of variation of the C/O^* ratio in the disk with respect to the other ratios, as it is shown in the bottom four panels of Figures 4–7 (note the different scales on the *y*-axes). The strongest effects on the planetary C/O^* ratio are observed in the two reset scenarios for gas-dominated giant planets, where the values decrease by a factor of 3 (i.e., from 1.6 to 0.5), for formation regions increasingly farther away from the star. In particular, the trend decreases steadily up to 50 au and progressively flattens further out. We discussed the origin of such a trend in Section 3.3. On the contrary, for both gas-dominated and solid-enriched giant planets, the C/N^* and N/O^* ratios are significantly more sensitive to the radial migration than the C/O^* ratio. Specifically, they show monotonic trends with deviations from the stellar value that increase with direct dependency on the migration, leading to separations up to one order of magnitude between short- and large-scale migrations.

The S/N^* ratio provides additional information for solid-enriched giant planets. As it is shown in the top-right panel of Figures 4–7, and highlighted in Figure 9, large-scale migrations of solid-enriched giant planets result in S/N^* ratios systematically above C/N^* ratios. Although the difference between the two may appear marginal, the trend results from the lower volatility of S with respect to C, which causes a larger fraction of S to be locked in the solid phase than C. Given that the total budget of S and C is dominated by the accretion of solids for large-scale migrations, the abundance of S grows faster than that of C, resulting in $S/N^* > C/N^*$. On the contrary, short-scale migrations of solid-enriched giant planets result in S/N^* ratios markedly lower than C/N^* ratios. Such a trend is a consequence of the increasingly dominant contribution of the gas accretion (see the discussion in Section 3.1) combined with the fact that the gas is the major carrier of C within the snowline of refractory organic carbon. Our results confirm that the relation between the S/N^* and C/N^* ratios holds for all the disk chemical scenarios in which the bulk of N remains in gaseous form while the bulk of S is early trapped in refractory

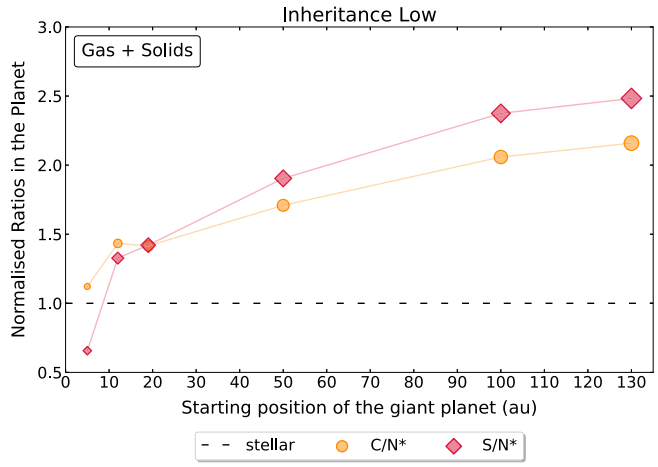

Figure 9. Comparison between the C/N^* and the S/N^* ratios of solid-enriched giant planets in the inheritance low scenario. The trends are taken from Figure 4 and shown in linear scale to highlight the differences. The black, dashed, horizontal line at 1 indicates the reference stellar value.

material, so that the planetary S/N^* ratio becomes a direct tracer of the planetesimal accretion.

Given its intrinsic properties, the S/N^* ratio is an extremely versatile diagnostic tool. In particular, the joint evaluation of the S/N^* ratio and the envelope metallicity of the planet allows discrimination between two scenarios that are not directly modeled by our simulations. The first one describes a giant planet that formed in situ and close to the star, in a hot environment with $T > 700$ K. At such a high temperature, all the volatile elements, including S, are in the gas phase. In cosmochemistry, S is indeed the most abundant among the moderately volatile elements (Palme et al. 2014), with condensation temperature $T_{\rm cond} = 672$ K (Wood et al. 2019). Consequently, the planet would be characterized by stellar values of both the envelope metallicity and the S/N^* ratio. The second scenario is that of a solid-enriched hot Jupiter that accreted most of its heavy-element budget beyond the N_2 snowline, where even the highly volatile molecules (CO and N_2) are condensed in the solid phase (Öberg & Wordsworth 2019). At the end of its migration, when the planet reaches its close-in orbit, its envelope would be characterized by a markedly superstellar metallicity and a stellar S/N^* ratio. Therefore, the joint evaluation of the metallicity and the S/N^* ratio allows distinguishing hot Jupiters that formed in situ and close to the star from those that underwent extreme migrations.

The combined use of metallicity, C/N^*, and S/N^* ratios allows the investigation of another alternative scenario that was not directly modeled by our simulations. This is the case of a giant planet that formed in a disk in which the inward drift of dust and pebbles causes the ices of C, O, and N to sublimate as they cross their respective snowlines (Booth & Ilee 2019; Schneider & Bitsch 2021), thus directly enriching the disk gas phase in heavy elements. In such scenario, gas accretion may then contribute more than solid accretion to the total metallicity of the planet, hence mimicking the effect of short-scale migration in our simulations. Due to the higher volatility of C with respect to S, sublimation would be more efficient in enriching the gas in C rather than in S. Therefore, hot Jupiters that form in such scenario, will be characterized by superstellar metallicity and $C/N^* > S/N^*$.

3.5. The Chemical Structure of the Birth Environment

As discussed in Sections 3.3 and 3.4, our new analysis confirms and expands the general conclusion of Paper I about the limited predictive power of the C/O^* ratio. Nevertheless, the C/O^* ratio does retain some diagnostic power in our model. Specifically, the C/O^* ratio of gas-dominated giant planets that underwent moderate and large-scale migrations (beyond 10 au in our model) is always superstellar in the inheritance scenarios and substellar in the reset ones (see the top-left panel in Figure 8). Therefore, provided that it is possible to independently unveil the origin of the accreted material, e.g., by looking at the other elemental ratios or through density and metallicity estimates, the C/O^* ratio of gas-dominated giant planets can be used to constrain the chemical structure of the birth environment. On the other hand, little can be said about solid-enriched giant planets, whose C/O^* ratio does not deviate appreciably from the stellar value in both scenarios.

For gas-dominated giant planets, the N/O^* ratio in the atmosphere provides additional insights into the chemical characterization of the disk. As it is shown in the bottom-left panel of Figure 8, the results for the inheritance and the reset scenarios follow two distinct trends that diverge with respect to each other. The separation between the two increases with the radial migration, resulting in a N/O^* ratio systematically higher in the inheritance scenarios than in the reset ones. Specifically, for large-scale migrations, the N/O^* ratio in the inheritance scenarios can be more than a factor of three larger than in the reset ones. Such a trend is a direct consequence of the higher abundance of gaseous O in the outer disk in the reset scenarios with respect to the inheritance ones (see Figure 3). We discussed this feature in Section 3.3 to explain why the C/O^* ratio of gas-dominated giant planets is substellar in the reset scenarios.

3.6. Pairwise Comparison of Elemental Ratios

To provide a more immediate visualization of the characteristics of planetary atmospheres and to facilitate the interpretation of observational data, we compared pairs of normalized elemental ratios through binary plots. Figure 10 illustrates this comparison for three pairs of ratios, C/N^* versus C/O^*, N/O^* versus C/O^*, and N/O^* versus C/N^* for both gas-dominated and solid-enriched giant planets in the four chemical scenarios. The gray dashed lines, indicating stellar values, delimit four quadrants in which the ratios can assume sub- or superstellar values. One of the advantages of this representation is that the results for different combinations of the parameters of the system (i.e., the extent of migration, the accretion, and chemical scenarios) occupy distinct quadrants. One can then immediately identify the conditions that favor one scenario over the others.

For instance, a point in the third quadrant (bottom left) of the C/N^* versus C/O^* plot, i.e., substellar values for both the C/N^* and C/O^* ratios, identifies a planet that started its migration far from the star (beyond the CO_2 snowline) and accreted only gas in a reset scenario. Conversely, a superstellar C/O^* ratio coupled with a C/N^* ratio an order of magnitude lower than the stellar value indicates that the same formation process occurred in an inheritance scenario.

Moreover, the comparison between the N/O^* and C/N^* ratios allows for constraining the accretion history and the migration of giant planets. Specifically, the deviations of the

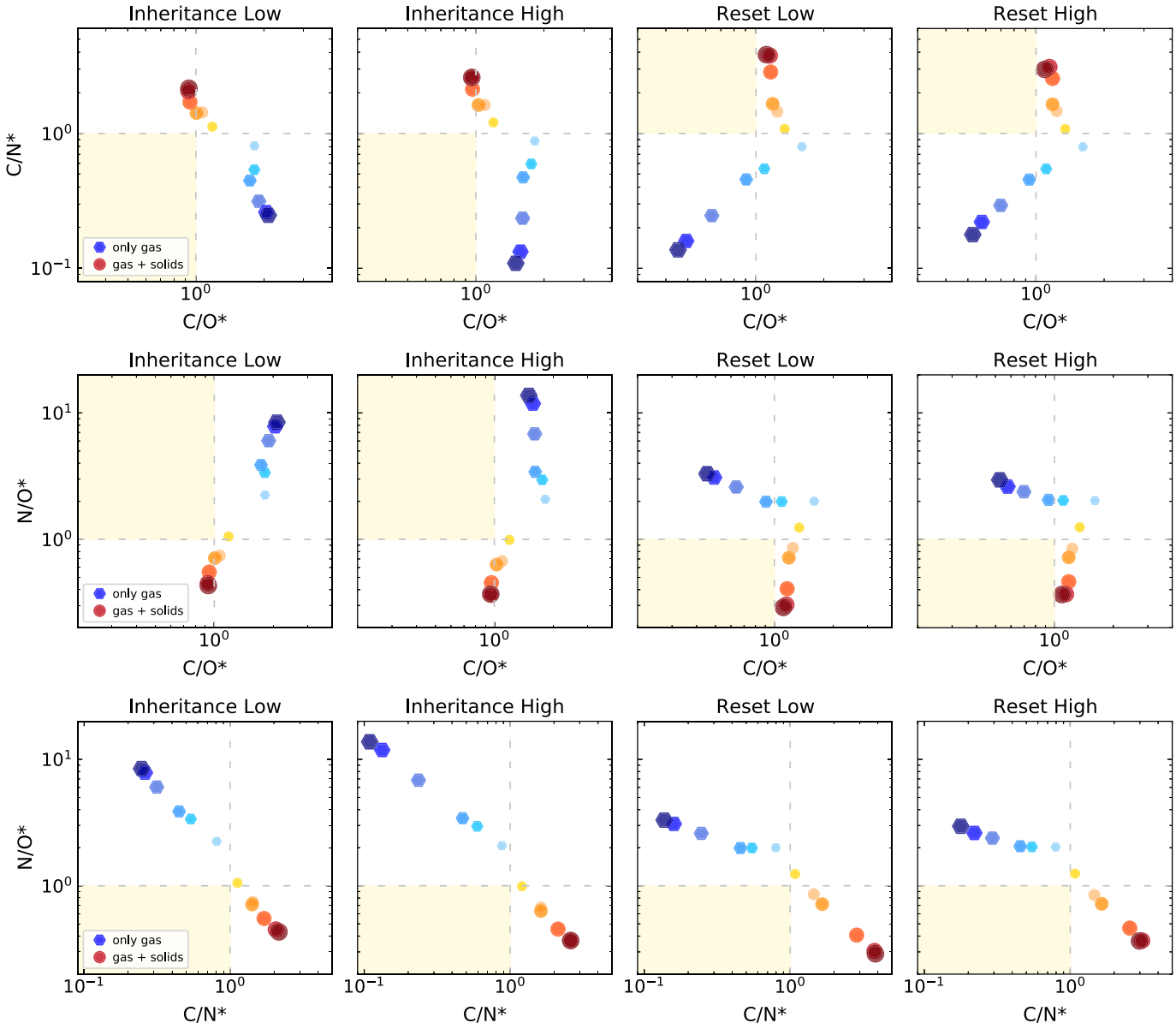

Figure 10. Comparison between pairs of normalized elemental ratios in the planet's atmosphere. Results are shown for the four analyzed chemical scenarios. Each point on the plots represents one of the six analyzed simulations, describing a planet that starts its migration at 5, 12, 19, 50, 100, and 130 au from the star. Color maps and increasing size of markers are used to distinguish between short-scale (light colors, small markers) and large-scale (dark colors, big markers) migrations. The blue markers (hexagons) indicate gas-dominated giant planets, while the red ones (circles) are for solid-enriched ones. The gray, dashed lines indicate stellar values. Their intersection identifies four quadrants in which the elemental ratios can assume sub- or superstellar values. The yellow shaded areas indicate regions of the parameter space that are forbidden in our simulations.

ratios from their respective stellar value are directly proportional to the radial migration and grow in opposite directions for gas-dominated and solid-enriched giant planets. In the inheritance scenarios (see the two bottom-left panels), the N/O^* and C/N^* ratios of gas-dominated giant planets can deviate up to one order of magnitude above and below the stellar value, respectively. For the same planets, moderate deviations of the N/O^* ratio with respect to the C/N^* ratio provide a strong indication that the evolution occurred in a reset scenario (see the two bottom-right panels). When considering solid-enriched giant planets, both the N/O^* and C/N^* ratios are less sensitive to migration than in gas-dominated planets and follow the same trend independently on the chemical scenario.

Alongside favored regions of the parameter space for the different planet formation histories, our results suggest forbidden (as indicated by the yellow shaded areas in Figure 10) or marginally permitted quadrants in pairwise elemental ratios analysis. For instance, in no case among those we investigated in our modeling can planets populate the quadrant where both the N/O^* and the C/N^* ratios are substellar (see the bottom four panels of Figure 10). The opposite case, i.e., N/O^* and C/N^* ratios simultaneously superstellar, is very marginally compatible only with solid-enriched giant planets that experienced very short-scale migrations, starting within the H_2O snowline.

3.7. Refractory Elements beyond S

One of the main findings of Paper I, confirmed by this study, is the untapped potential of the S/N^* ratio as a diagnostic tool for planet formation. As discussed in Section 3.4, this is

essentially due to the marked volatility contrast between S and N, which makes their ratio an effective tracer of the accretion of solids. It is important to point out, however, that any element X more refractory than O can be used in place of S to perform the same analysis. From an observational perspective, this means that our set of diagnostic tracers can be extended to elements that may be more easily detectable than others in giant planet atmospheres. For instance, for increasing equilibrium temperatures of the planets, the atmospheres get enriched in elements with increasingly lower volatility. For warm and hot Jupiters, moderately volatile elements are all good alternatives to S. Such category includes elements that condense at temperatures between 1250 K and 250 K, such as Na, K, Cl, and F (Palme et al. 2014; Wood et al. 2019). For ultrahot Jupiters the list extends to refractory (e.g., Al, Ca, and Ti) and rock-forming (e.g., Mg, Si, Ni, and Fe) elements, which have condensation temperatures in the range 1850–1250 K (Palme et al. 2014; Wood et al. 2019).

In Section 3.4 we stressed that the planetary elemental ratios strongly depend on the phase of the main carrier of the two involved elements (e.g., the gas phase for N_2, which is the main carrier of N and the solid phase for the rocks that are the main reservoir of S) and on how efficiently the gas and the solids contribute to the final envelope metallicity. In particular, we examined the case of the C/N^* and S/N^* ratios in solid-enriched giant planets. Which of the two ratios is larger than the other depends on whether the planet's formation is dominated by the accretion of gas or solids. More generally, the comparison between two elemental ratios X/N^* and Y/N^*, where the elements X and Y have a marked volatility contrast, allows for discrimination between scenarios in which one of the two elements is predominantly accreted by different phases.

In Section 3.4 we also highlighted that the S/N^* ratio allows to resolve scenarios of in situ formation very close to the star, in a hotter environment than the condensation temperature of S. Specifically, giant planets that formed by accreting gas from such a region will be characterized by stellar values of both metallicity and S/N^* ratio. It is important to notice that the replacement of S with a more refractory element would push this limit toward higher temperatures, allowing to resolve formation scenarios even closer to the star.

In Section 3.4 we also discussed how the comparison between the metallicity and the C/N^* and S/N^* ratios allows the identification of giant planets that formed by accreting gas enriched in heavy elements due to the sublimation of inwardly drifting dust and pebbles, contrary to planetesimal accretion. Sublimation is more efficient in enriching giant planets in highly volatile elements rather than in refractory ones. In particular, any refractory element X would produce less enrichment in the gas than in C. Therefore, planets that formed by accreting high-metallicity gas would be characterized by superstellar metallicity and $C/N^* > X/N^*$.

3.8. Linking Our Predictions to Observable Planetary Atmospheres

In the previous sections we discussed how the atmospheric elemental ratios can be used to trace the formation history of giant planets. From an observational perspective, such elemental ratios need to be retrieved from the abundances of the molecular carriers of C, O, N, and S in exoplanetary atmospheres.

The observable chemistry in giant planet atmospheres is shaped by multiple and diverse processes, such as thermochemical reactions at equilibrium, mixing processes, photochemistry, and chemical diffusion. Each of them dominates in different atmospheric layers (e.g., Madhusudhan et al. 2016 and references therein).

Deep in the atmosphere, the chemistry is at equilibrium and the chemical composition is a function only of the elemental abundances, the temperature, and the pressure. For a solar composition, the main molecular carriers of C and N are CO, CH_4, N_2, and NH_3. Two regimes in the pressure–temperature space can be identified. At high temperatures and low pressures, C and N are essentially locked in CO and N_2, while at low temperatures and high pressures, the main reservoirs of C and N are CH_4 and NH_3. At the pressure of 1 bar, the transition between the two regimes occurs at temperatures of 1200 K and 700 K for the C- and N-bearing molecules, respectively. O is largely present as water vapor, while S is mainly locked into H_2S (e.g., Madhusudhan et al. 2016; Fortney et al. 2021 and references therein). The chemical equilibrium in atmospheres with supersolar metallicity generally favors the production of molecules that contain two or more heavy elements. In such atmospheres, CO_2 is therefore favored over CO and N_2, which in turn are favored over CH_4 and NH_3 (e.g., Madhusudhan et al. 2016 and references therein).

In the upper layers of the atmosphere, photochemical reactions induced by stellar UV radiation are proved to alter the chemical composition. Among the direct and indirect products of photochemistry there are H, HCN, C_2H_2, OH, O_2, and NO. Regarding S, photochemistry converts H_2S in S, HS, S_2, SO, and SO_2 (e.g., Madhusudhan et al. 2016; Fortney et al. 2021).

Chemistry in observed exoplanetary atmospheres may be more complex than discussed above, being also influenced by the cooling history of the planet (Fortney et al. 2020). At intermediate layers, volatile species may be sequestered into clouds, although these are not expected to form at the high atmospheric temperatures of hot Jupiters (e.g., Madhusudhan et al. 2016; Madhusudhan 2019 and references therein).

Ground-based and high-resolution spectral observations have recently succeeded in providing the first characterizations of exoplanetary atmospheres. For instance, observations by Giacobbe et al. (2021) of the hot Jupiter HD 209458b, at the equilibrium temperature of 1500 K, revealed the presence of H_2O, CO, HCN, CH_4, NH_3, and C_2H_2 in the atmosphere. Carleo et al. (2022) and Guilluy et al. (2022) have recently extended this result to giant planets with equilibrium temperature $T \leqslant 1000$ K. Future observations with JWST (Greene et al. 2016), Twinkle (Edwards et al. 2019b), and Ariel (Tinetti et al. 2018), as well as advances in atmospheric retrieval techniques, will soon revolutionize the field. The broad spectral range and the high spectral resolution of JWST will allow for precise determination of the abundances of a number of species of interest besides H_2O, like CO, CO_2, CH_4, and NH_3 (Greene et al. 2016). An even greater number of molecules will be accessible with Ariel, by the time the telescope starts its operations in 2029 (Tinetti et al. 2018).

Recent studies have validated our methodology on real data in preparation of its use for interpreting the observations of future ground-based and space-based facilities. Alongside Carleo et al. (2022) and Guilluy et al. (2022), Biazzo et al. (2022)

put constraints on possible formation scenarios for the giant planets in four planetary systems, around the stars HAT-P-26, WASP-39, HAT-P-12, and WASP-10. Specifically, they analyzed the trends of the normalized planetary metallicity and elemental ratios based on the atmospheric composition obtained by Kawashima & Min (2021) through spectral disequilibrium retrieval models. A similar study was performed independently by Kolecki & Wang (2022) on an additional set of four giant planets. As discussed before, Carleo et al. (2022) and Guilluy et al. (2022) jointly used the planetary metallicity and the C/O^* ratio to constrain the formation histories of WASP-69b and WASP-80b, as well as the characteristics of their native circumstellar disks (see also Section 3.3). More systematic studies of the observational implications of our results will be the focus of dedicated future works.

4. Conclusions

In this work, we investigated the link between the final composition of the atmospheres of giant planets and their formation process, focusing on the effects of different chemical initial conditions for the host protoplanetary disk. The study in Paper I was limited to a disk that inherited its composition from the prestellar core and whose chemical evolution was limitedly affected by cosmic rays and similar energy sources. Here we also explored the case of a complete reset of the chemistry, as well as the impact of different levels of the ionization rate throughout the disk. Specifically, we considered a first case in which the only source of ionization is the decay of short-lived radionuclides (i.e., the same considered in Paper I) and a second case in which an additional contribution is provided by cosmic rays. In addition, we introduced a more realistic model of the condensation of refractory organic carbon.

We analyzed the six *N*-body simulations from Paper I of the growth and migration of a giant planet in a disk of gas and planetesimals. During the migration, the planet grows in radius and mass by accreting gas and solids characterized by different compositions and relative abundances of refractory and volatile elements. By coupling the outcome of the simulations with the different compositional models of the disk we derived the composition of the accreted material, from which we computed the C/O, N/O, C/N, and S/N ratios in the final atmosphere of the planet. For a better interpretation of the results, we normalized the elemental ratios to their corresponding stellar values and we indicated the new values with the superscript *. Our findings can be summarized as follows:

1. The final composition of giant planets is markedly nonstellar due to the interplay between planetary migration and concurrent accretion of gas and solids. Therefore, despite being intimately connected, the planetary elemental ratios are not a direct reflection of those of the disk.
2. The diagnostic power of the elemental ratios is maximized when these are expressed in units of their corresponding stellar value. First, normalization brings different elemental ratios to the same scale, making it easier to compare them and study their mutual relations. As discussed below, such relations provide unique insights into the formation and migration histories of giant planets. Second, normalization allows us to directly measure the deviation of the planet's composition from that of its host star, which in turn reflects the original composition of the formation environment. As a result, we can constrain the formation history of the planet even in the absence of detailed knowledge of the specific properties of the natal environment. The use of normalized elemental ratios is therefore key to comparing the formation histories of giant planets in multiplanet systems and of giant planets orbiting different stars.
3. In all the disk chemical scenarios, the joint evaluation of C- and N-based elemental ratios allows the unequivocal constraining of the source of planetary metallicity. Specifically, gas-dominated giant planets are characterized by $N/O^* > C/O^* > C/N^*$, while solid-enriched giant planets are characterized by $C/N^* > C/O^* > N/O^*$. Moreover, all the planetary elemental ratios, except C/O^*, exhibit monotonic trends with respect to the starting location of the planet. Specifically, the deviation of the ratios from their stellar value increases with the extent of disk-driven migration, independent of the disk chemical scenario and the ionization level.
4. The global trends of the elemental ratios in the planet composition through the different migration scenarios are not model-dependent—only their absolute values are. Specifically, changing the chemical and thermal profiles of the disk only affects the slope of the curves shown in our plots, but not their overall behavior, as verified by Biazzo et al. (2022). Therefore, our methodology can be directly applied to compare the formation and migration histories of different giant planets in the same planetary system.
5. For solid-enriched giant planets, the C/O^* ratio provides constraints only on the accretion scenario, as its value changes limitedly with migration. For gas-dominated ones, it can also provide information on the chemical structure of the disk, although this is true only for large-scale migration scenarios.
6. For gas-dominated giant planets, the joint evaluation of the N/O^* and the C/O^* ratios allows the constraining of the disk chemical scenario. Specifically, the N/O^* ratio is up to a factor of 3 higher in the inheritance scenarios than in the reset ones. In parallel, for large-scale migrations the C/O^* ratio is superstellar in the inheritance scenarios and substellar in the reset ones. The elemental ratios of solid-enriched giant planets are instead limitedly affected by whether the disk is characterized by chemical inheritance or reset, making it hard to discriminate between the two scenarios.
7. The S/N^* ratio provides additional constraints on the migration history of solid-enriched giant planets. Specifically, large-scale migrations associated with substantial accretion of solids result in $S/N^* > C/N^*$. On the contrary, short-scale migrations associated with a limited supply of solids and increased contribution of gas accretion result in $S/N^* < C/N^*$. Such relations hold for all the disk chemical scenarios in which the bulk of N remains in gaseous form while the bulk of S is early trapped in refractory material, so that the planetary S/N^* ratio becomes a direct tracer of the planetesimal accretion.
8. Given the high volatility contrast between S and N, the joint evaluation of the planetary S/N^* ratio and metallicity allows for the distinguishing of hot Jupiters that formed in situ and close to the star from those that

underwent extreme migrations, from beyond the snowline of N_2. The first will be characterized by stellar values of both the metallicity and the S/N^* ratio, while the second will have a markedly superstellar metallicity and stellar S/N^* ratio. The metallicity, combined with the C/N^* and the S/N^* ratios, also allows the tracing of the formation histories of giant planets in disks whose gas phase is enriched in heavy elements due to the sublimation of inwardly drifting dust and pebbles. Such planets will be characterized by superstellar envelope metallicity and $C/N^* > S/N^*$.

9. Pairwise comparison of multiple normalized elemental ratios provides additional insights into the planet formation history and the chemical initial conditions of the disk. The associated binary plots allow us to immediately identify the conditions that favor one scenario over the others, hence providing an effective tool for the interpretation of observational data.

The authors wish to thank Aldo Bonomo, Gloria Guilluy, and Ilaria Carleo for their discussion and feedback on exoplanetary atmospheric observations. The authors acknowledge the support of the European Research Council via the Horizon 2020 Framework Programme ERC Synergy "ECOGAL" Project GA-855130, of the Italian National Institute of Astrophysics (INAF) through the INAF Main Stream project "Ariel and the astrochemical link between circumstellar disks and planets" (CUP: C54I19000700005), and of the Italian Space Agency (ASI) through the ASI-INAF contract No. 2021-5-HH.0. The authors also acknowledge the contribution from PRIN INAF 2019 through the project "HOT-ATMOS." The computational resources for this work were supplied by the Genesis cluster at INAF-IAPS and the technical support of Scigé John Liu is gratefully acknowledged.

Appendix
Planet Formation Simulations

The *N*-body simulations performed in Paper I investigate the gas and planetesimal accretion histories of giant planets starting their formation tracks at different radial distances from the host star, within their native protoplanetary disk. The initial orbital regions of the giant planets were chosen to explore the possible compositional signatures of the extended planet-forming regions revealed by recent ALMA surveys (see Section 2 and Paper I for discussion and references). The *N*-body simulations were performed with the parallel *N*-body code Mercury-Arχes (Turrini et al. 2019, 2021), which accounts for the effects of the disk gas on the dynamical evolution of the planetesimals and implements a two-phase approach to model both the mass growth and the migration of the forming planets. This two-phase approach is modeled after the growth and migration tracks from Bitsch et al. (2015), D'Angelo et al. (2021), and Mordasini et al. (2015). The numerical treatment of the physical effects accounted for by Mercury-Arχes is summarized here.

The first phase corresponds to the growth of the core and the accretion of its extended atmosphere. During this first phase the giant planet is assumed to undergo migration according to a damped Type I regime. The second phase corresponds to the runaway gas accretion and the decrease of the planetary radius due to the gas infall. During this second phase the giant planet migrates first by full Type I migration followed by Type II migration. The equations governing the evolution of the giant planet during these two phases are described in chronological order the following.

During the first phase of core growth, the planetary mass grows from a Mars-like planetary embryo ($M_0 = 0.1\,M_\oplus$) to a critical value of $M_c = 30\,M_\oplus$, following the growth curve (Turrini et al. 2011):

$$M_1(t) = M_0 + \left(\frac{e}{e-1}\right)(M_c - M_0)(1 - e^{-t/\tau_c}), \quad \text{(A1)}$$

where τ_c is the duration of the first growth phase, set to 2 Myr. In parallel, the planetary radius grows following the treatment for extended atmospheres of Fortier et al. (2013), based on the hydrodynamical simulations of Lissauer et al. (2009), as:

$$R_1(t) = \frac{G\,M_1(t)}{c_s^2/k_1 + G\,M_1(t)/(k_2 R_H)}, \quad \text{(A2)}$$

where G is the gravitational constant, c_s is the speed of sound in the protoplanetary disk at the orbital distance of the planet, R_H is the planetary Hill's radius, $k_1 = 1$, and $k_2 = 1/4$ (Lissauer et al. 2009). The initial orbit of the giant planet is planar ($i = 0°$) and characterized by low eccentricity ($e = 10^{-3}$). The damped Type I migration of the giant planet is described by the drift rate (Hahn & Malhotra 2005; Walsh et al. 2011; Turrini et al. 2021):

$$\Delta v_1 = \frac{1}{2}\frac{\Delta a_1}{a_p}\frac{\Delta t}{\tau_c} v_p, \quad \text{(A3)}$$

where Δt is the timestep of the *N*-body simulation, Δa_1 is the radial displacement during the growth of the core, and v_p and a_p are the instantaneous planetary orbital velocity and semimajor axis, respectively. In all *N*-body simulations Δa_1 accounts for 40% of the total radial displacement (Mordasini et al. 2015; Turrini et al. 2021).

During the second phase of runaway gas accretion, the planetary mass evolves as (Turrini et al. 2011):

$$M_2(t) = M_c + (M_F - M_c)(1 - e^{-(t-\tau_c)/\tau_g}), \quad \text{(A4)}$$

where M_F is the final mass of the giant planet set to 317.8 $M_\oplus$, i.e., the Jovian mass, and τ_g is the e-folding time of the runaway gas accretion process. The value of τ_g is set to 0.1 Myr based on the results of hydrodynamical simulations (Lissauer et al. 2009; D'Angelo et al. 2021), meaning that the gas giant reaches more than 99% of its final mass in about 0.5 Myr from the onset of the runaway gas accretion. Once the giant planet enters the runaway gas accretion phase (i.e., for $t > \tau_c$), the gravitational infall of the gas causes the planetary radius to shrink and evolve as:

$$R_2(t) = R_E - \Delta R(1 - \exp^{-(t-\tau_c)/\tau_g}), \quad \text{(A5)}$$

where $R_E = R_1(\tau_c)$ is the planetary radius at the end of the core growth phase and $\Delta R = R_E - R_I$ is the decrease of the planetary radius during the gravitational collapse of the gas. R_I is the final inflated radius of the young and hot giant planet assumed to be equal to 1.6 R_J, where R_J is the Jovian radius, based on the hydrodynamical simulations by Lissauer et al. (2009) and D'Angelo et al. (2021). While in this second formation phase, the migrating giant planet transitions to a full Type I regime and Type II regime, and its drift rate is (Hahn & Malhotra 2005;

Shibata et al. 2020; Turrini et al. 2021):

$$\Delta v_2 = \frac{1}{2}\frac{\Delta a_2}{a_p}\frac{\Delta t}{\tau_g}\exp^{-(t-\tau_c)/\tau_g} v_p, \quad \text{(A6)}$$

where Δa_2 is the radial displacement during the runaway gas accretion. In all N-body simulations Δa_2 accounts for 60% of the total radial displacement (Mordasini et al. 2015; Turrini et al. 2021).

The circumstellar disk considered in the N-body simulations of Paper I is modeled adopting the surface density profile of the protoplanetary disk surrounding the A-type star HD 163296 (Isella et al. 2016), one of the most studied and best-characterized disks to date (e.g., Turrini et al. 2021, 2022, and references therein). The circumstellar disk has characteristic radius $r_c = 165$ au and gas surface density:

$$\Sigma(r) = \Sigma_0 (r/r_c)^{\gamma} exp[-(r/r_c)^{(2-\gamma)}], \quad \text{(A7)}$$

where $\gamma = 0.8$ (Isella et al. 2016). As HD 163296 is more massive than the Sun, the Σ_0 value was scaled down to 3.3835 g cm^{-3} so that the total disk mass matches that of a minimum mass solar nebula (Hayashi 1981) with the same radial extension, i.e., $M_* = 0.053\ M_\odot$. The disk gas mass is assumed in steady state and does not decline over time. The inner edge of the disk is set to 0.1 au in all simulations. The disk temperature profile on the midplane is $T(r) = T_0\, r^{-0.6}$, where $T_0 = 200$ K (Andrews & Williams 2007; Öberg et al. 2011; Eistrup et al. 2016).

During the runaway gas accretion phase, the giant planet forms a gap in the disk gas whose width is modeled as $W_{gap} = C \cdot R_H$ (Isella et al. 2016; Marzari 2018), where the numerical proportionality factor $C = 8$ is taken from Isella et al. (2016) and Marzari (2018). The gas density $\Sigma_{gap}(r)$ inside the gap evolves over time with respect to the local unperturbed gas density $\Sigma(r)$ as $\Sigma_{gap}(r) = \Sigma(r) \cdot \exp[-(t - \tau_c)/\tau_g]$, where τ_c and τ_g are the same as in Equations (A1) and (A4) (Turrini et al. 2021).

Planetesimals embedded in the disk gas are affected by both the aerodynamic drag of the gas and the disk self-gravity (Weidenschilling 1977; Ward 1981; Armitage 2009). The gas drag acceleration F_D is expressed by:

$$F_D = \frac{3}{8}\frac{C_D}{r_p}\frac{\rho_g}{\rho_p} v_r^2, \quad \text{(A8)}$$

where C_D is the gas drag coefficient, ρ_g is the local density of the gas, ρ_p, and r_p are, respectively, the density and radius of the planetesimals, and v_r is the relative velocity between the gas and the planetesimals (Weidenschilling 1977; Armitage 2009). The gas drag coefficient C_D is computed following the treatment described by Nagasawa et al. (2019) as a function of the Reynolds (Re) and Mach (Ma) numbers, to account for both subsonic and supersonic regimes of motion of the planetesimals:

$$C_D = \left[\left(\frac{24}{Re} + \frac{40}{10 + Re}\right)^{-1} + 0.23\, Ma\right]^{-2} + \frac{2 \cdot (0.8\, k + Ma)}{1.6 + Ma},$$

where k is equal to 0.4 for $Re < 10^5$ and to 0.2 for $Re > 10^5$ (Nagasawa et al. 2019).

The exciting effect of the disk self-gravity is modeled following the approach of Nagasawa et al. (2019), based on the analytical treatment for axisymmetric thin disks from Ward (1981), whose accuracy has been validated by the hydrodynamical study of Fontana & Marzari (2016). The force due to the disk self-gravity (F_{SG}) is given by:

$$F_{SG} = 2\pi\ G\ \Sigma(r) \sum_{n=0}^{\infty} A_n \frac{(1-k)(4n+1)}{(2n+2-k)(2n-1+k)}, \quad \text{(A9)}$$

where $k = 0.8$ is the exponent of the power law in Equation (A7) and $A_n = [(2n)!\ /\ 2^{2n}(n!)^2]^2$ (Ward 1981; Marzari 2018). For this value of k the sum on the right hand of Equation (A9) converges to the value -0.754126 and Equation (A9) becomes:

$$F_{SG} = Z\pi G\Sigma(r), \quad \text{(A10)}$$

where $Z = -1.508252$ (see Turrini et al. 2021 and Marzari 2018 for further discussion).

Planetesimals are included in the N-body simulations as test particles that do not interact with each other nor influence the dynamical evolution of the forming giant planet, i.e., they do not possess gravitational mass. The test particles are dynamically affected by the giant planet, the central star, and the gas in the circumstellar disk. To properly compute the effect of the gas drag, we attribute the test particles inertial masses computed assuming a characteristic radius of 100 km (Klahr & Schreiber 2016; Johansen & Lambrechts 2017; Pirani et al. 2019) and density values of 2.4 and 1.0 g cm^{-3} depending on whether the planetesimals originated within or beyond the water snowline (see Turrini et al. 2018, 2021 for the physical justification of the adopted values and see below for the implications of the choice of the characteristic size of the planetesimals). The test particles are initially on low eccentricity and low inclination orbits ($e \approx i \leqslant 10^{-2}$), and they uniformly sample the radial extension of the disk between 1 au and the disk radius r_c, with a spatial density of 2000 particles/au. Particles that encounter the giant planet at a distance closer than the planetary radius at the time of the encounter are considered to be accreted by the planet (see Turrini et al. 2021 and Podolak et al. (2020) for additional discussion). See Section 2 and Turrini et al. (2021) for a discussion of the accreted mass associated to each close encounter. We refer the reader to Figure 1 and to its animated version in the online journal for a visualization of the planet formation process modeled by our simulations.

The migration tracks adopted in the N-body simulations of Paper I and described above are not unique, and the migration histories of giant planets can be associated with different migration rates (see also Pirani et al. 2019). Similarly, planetesimal disks are characterized by continuous size-frequency distributions of the planetesimals (see, e.g., Krivov et al. 2018; Turrini et al. 2019, and references therein) rather than a single characteristic size. However, the investigation of Shibata et al. (2020) shows that changes in the migration rate and in the size of the planetesimals translate into an enhancement or a reduction of the planetesimal flux on the giant planet. Specifically, faster migration rates and larger planetesimal sizes increase the planetesimal accretion flux, while slower migration rates and smaller planetesimal radii have the opposite effect. Consequently, changes in these two parameters only affect the planetesimal accretion fluxes quantitatively and not qualitatively (see Shibata et al. 2020

for additional discussion). Furthermore, since realistic planetesimal populations are dominated in mass by the high-end tail of their size-frequency distribution (see, e.g., Krivov et al. 2018; Turrini et al. 2019, for discussion), the choice of adopting the planetesimal characteristic radius of 100 km in the simulations of Paper I instead of larger values means that the planetesimal fluxes computed from these simulations are conservative estimates.

ORCID iDs

Elenia Pacetti https://orcid.org/0000-0003-1096-7656
Diego Turrini https://orcid.org/0000-0002-1923-7740
Eugenio Schisano https://orcid.org/0000-0003-1560-3958
Sergio Molinari https://orcid.org/0000-0002-9826-7525
Sergio Fonte https://orcid.org/0000-0002-3911-7340
Romolo Politi https://orcid.org/0000-0002-9793-9780
Patrick Hennebelle https://orcid.org/0000-0002-0472-7202
Ralf Klessen https://orcid.org/0000-0002-0560-3172
Leonardo Testi https://orcid.org/0000-0003-1859-3070
Ugo Lebreuilly https://orcid.org/0000-0001-8060-1890

References

Allègre, C., Manhès, G., & Lewin, É. 2001, E&PSL, 185, 49
ALMA Partnership, Brogan, C. L., Pérez, L. M., et al. 2015, ApJ, 808, L3
Altwegg, K., Balsiger, H., & Fuselier, S. A. 2019, ARA&A, 57, 113
Andrews, S. M., Huang, J., Pérez, L. M., et al. 2018, ApJL, 869, L41
Andrews, S. M., & Williams, J. P. 2007, ApJ, 659, 705
Armitage, P. J. 2009, Astrophysics of Planet Formation (Cambridge: Cambridge Univ. Press)
Asplund, M., Grevesse, N., Sauval, A. J., & Scott, P. 2009, ARA&A, 47, 481
Bardyn, A., Baklouti, D., Cottin, H., et al. 2017, MNRAS, 469, S712
Barstow, J. K., Changeat, Q., Garland, R., et al. 2020, MNRAS, 493 4884
Bergin, E. A., Blake, G. A., Ciesla, F., Hirschmann, M. M., & Li, J. 2015, PNAS, 112, 8965
Bernabò, L. M., Turrini, D., Testi, L., Marzari, F., & Polychroni, D. 2022, ApJL, 927, L22
Bianchi, E., Codella, C., Ceccarelli, C., et al. 2019, MNRAS, 483, 1850
Biazzo, K., D'Orazi, V., Desidera, S., et al. 2022, A&A, 664, A161
Bitsch, B., Lambrechts, M., & Johansen, A. 2015, A&A, 582, A112
Booth, R. A., & Ilee, J. D. 2019, MNRAS, 487, 3998
Boss, A. P., Fisher, R. T., Klein, R. I., & McKee, C. F. 2000, ApJ, 528, 325
Brasser, R., Duncan, M. J., & Levison, H. F. 2007, Icar, 191, 413
Carleo, I., Giacobbe, P., Guilluy, G., et al. 2022, AJ, 164, 101
Chambers, J. E. 1999, MNRAS, 304, 793
Cleeves, L. I., Adams, F. C., & Bergin, E. A. 2013a, ApJ, 772, 5
Cleeves, L. I., Adams, F. C., Bergin, E. A., & Visser, R. 2013b, ApJ, 777, 28
Cleeves, L. I., Bergin, E. A., & Adams, F. C. 2014, ApJ, 794, 123
Cridland, A. J., van Dishoeck, E. F., Alessi, M., & Pudritz, R. E. 2019, A&A, 632, A63
Currie, T., Lawson, K., Schneider, G., et al. 2022, NatAs, 6, 751
D'Angelo, G., Weidenschilling, S. J., Lissauer, J. J., & Bodenheimer, P. 2021, Icar, 355, 114087
Delgado Mena, E., Israelian, G., González Hernández, J. I., et al. 2010, ApJ, 725, 2349
Drazkowska, J., Bitsch, B., Lambrechts, M., et al. 2022, arXiv:2203.09759
Drozdovskaya, M. N., van Dishoeck, E. F., Rubin, M., Jørgensen, J. K., & Altwegg, K. 2019, MNRAS, 490, 50
Edwards, B., Mugnai, L., Tinetti, G., Pascale, E., & Sarkar, S. 2019a, AJ, 157, 242
Edwards, B., Rice, M., Zingales, T., et al. 2019b, ExA, 47, 29
Eistrup, C., Walsh, C., & van Dishoeck, E. F. 2016, A&A, 595, A83
Ercolano, B., & Glassgold, A. E. 2013, MNRAS, 436, 3446
Fedele, D., Carney, M., Hogerheijde, M. R., et al. 2017, A&A, 600, A72
Fedele, D., Tazzari, M., Booth, R., et al. 2018, A&A, 610, A24
Fontana, A., & Marzari, F. 2016, A&A, 589, A133
Fortier, A., Alibert, Y., Carron, F., Benz, W., & Dittkrist, K. M. 2013, A&A, 549, A44
Fortney, J. J., Dawson, R. I., & Komacek, T. D. 2021, JGRE, 126, e06629
Fortney, J. J., Visscher, C., Marley, M. S., et al. 2020, AJ, 160, 288
Giacobbe, P., Brogi, M., Gandhi, S., et al. 2021, Natur, 592, 205
Greene, T. P., Line, M. R., Montero, C., et al. 2016, ApJ, 817, 17
Guilluy, G., Giacobbe, P., Carleo, I., et al. 2022, arXiv:2207.09760
Hahn, J. M., & Malhotra, R. 2005, AJ, 130, 2392
Hayashi, C. 1981, PThPS, 70, 35
Isella, A., Guidi, G., Testi, L., et al. 2016, PhRvL, 117, 251101
Isnard, R., Bardyn, A., Fray, N., et al. 2019, A&A, 630, A27
Johansen, A., & Lambrechts, M. 2017, AREPS, 45, 359
Kawashima, Y., & Min, M. 2021, A&A, 656, A90
Klahr, H., & Schreiber, A. 2016, in IAU Symp. 318, Asteroids: New Observations, New Models, ed. S. R. Chesley (Cambridge: Cambridge Univ. Press), 1
Kolecki, J. R., & Wang, J. 2022, AJ, 164, 87
Krivov, A. V., Ide, A., Löhne, T., Johansen, A., & Blum, J. 2018, MNRAS, 474, 2564
Le Roy, L., Altwegg, K., Balsiger, H., et al. 2015, A&A, 583, A1
Lee, J.-E., Bergin, E. A., & Nomura, H. 2010, ApJL, 710, L21
Lichtenberg, T., Schaefer, L. K., Nakajima, M., & Fischer, R. A. 2022, arXiv:2203.10023
Lissauer, J. J., Hubickyj, O., D'Angelo, G., & Bodenheimer, P. 2009, Icar, 199, 338
Lodders, K. 2010, ASSP, 16, 379
Long, F., Pinilla, P., Herczeg, G. J., et al. 2018, ApJ, 869, 17
Lothringer, J. D., Rustamkulov, Z., Sing, D. K., et al. 2021, ApJ, 914, 12
Madhusudhan, N. 2019, ARA&A, 57, 617
Madhusudhan, N., Agúndez, M., Moses, J. I., & Hu, Y. 2016, SSRv, 205, 285
Magrini, L., Danielski, C., Bossini, D., et al. 2022, A&A, 663, A161
Manara, C. F., Morbidelli, A., & Guillot, T. 2018, A&A, 618, L3
Marzari, F. 2018, A&A, 611, A37
Meijerink, R., Aresu, G., Kamp, I., et al. 2012, A&A, 547, A68
Mordasini, C., Mollière, P., Dittkrist, K. M., Jin, S., & Alibert, Y. 2015, IJAsB, 14, 201
Mordasini, C., van Boekel, R., Mollière, P., Henning, T., & Benneke, B. 2016, ApJ, 832, 41
Mulders, G. D. 2018, in Handbook of Exoplanets, ed. H. J. Deeg & J. A. Belmonte (Cham: Springer), 153
Mulders, G. D., Pascucci, I., Ciesla, F. J., & Fernandes, R. B. 2021, ApJ, 920, 66
Nagasawa, M., Tanaka, K. K., Tanaka, H., et al. 2019, ApJ, 871, 110
Öberg, K. I., & Bergin, E. A. 2021, PhR, 893, 1
Öberg, K. I., Murray-Clay, R., & Bergin, E. A. 2011, ApJL, 743, L16
Öberg, K. I., & Wordsworth, R. 2019, AJ, 158, 194
Padovani, M., Ivlev, A. V., Galli, D., & Caselli, P. 2018, A&A, 614, A111
Padovani, M., Marcowith, A., Hennebelle, P., & Ferrière, K. 2016, A&A, 590, A8
Palme, H., Lodders, K., & Jones, A. 2014, in Treatise on Geochemistry, ed. H. D. Holland & K. K. Turekian, Vol. 2 (Oxford: Elsevier), 15
Pinte, C., Price, D. J., Ménard, F., et al. 2018, ApJL, 860, L13
Pirani, S., Johansen, A., Bitsch, B., Mustill, A. J., & Turrini, D. 2019, A&A, 623, A169
Podolak, M., Haghighipour, N., Bodenheimer, P., Helled, R., & Podolak, E. 2020, ApJ, 899, 45
Pollack, J. B., Hubickyj, O., Bodenheimer, P., et al. 1996, Icar, 124, 62
Rab, C., Güdel, M., Woitke, P., et al. 2018, A&A, 609, A91
Raymond, S. N., Kokubo, E., Morbidelli, A., Morishima, R., & Walsh, K. J. 2014, in Protostars and Planets VI, ed. H. Beuther et al. (Tucson, AZ: Univ. Arizona Press), 595
Rodgers-Lee, D., Taylor, A. M., Downes, T. P., & Ray, T. P. 2020, MNRAS, 491, 4742
Rubin, M., Altwegg, K., Balsiger, H., et al. 2019, MNRAS, 489, 594
Rubin, M., Engrand, C., Snodgrass, C., et al. 2020, SSRv, 216, 102
Schneider, A. D., & Bitsch, B. 2021, A&A, 654, A72
Schwarz, K. R., & Bergin, E. A. 2014, ApJ, 797, 113
Scott, E. R. D. 2007, AREPS, 35, 577
Scott, P., Asplund, M., Grevesse, N., Bergemann, M., & Sauval, A. J. 2015a, A&A, 573, A26
Scott, P., Grevesse, N., Asplund, M., et al. 2015b, A&A, 573, A25
Shibata, S., Helled, R., & Ikoma, M. 2020, A&A, 633, A33
Sotiriadis, S., Libert, A.-S., & Raymond, S. N. 2018, A&A, 613, A59
Testi, L., Natta, A., Manara, C. F., et al. 2022, A&A, 663, A98
Thiabaud, A., Marboeuf, U., Alibert, Y., et al. 2014, A&A, 562, A27
Tinetti, G., Drossart, P., Eccleston, P., et al. 2018, ExA, 46, 135

Turrini, D., Codella, C., Danielski, C., et al. 2022, ExA, 53, 225
Turrini, D., Magni, G., & Coradini, A. 2011, MNRAS, 413, 2439
Turrini, D., Marzari, F., Polychroni, D., & Testi, L. 2019, ApJ, 877, 50
Turrini, D., Miguel, Y., Zingales, T., et al. 2018, ExA, 46, 45
Turrini, D., Schisano, E., Fonte, S., et al. 2021, ApJ, 909, 40
Walsh, K. J., Morbidelli, A., Raymond, S. N., O'Brien, D. P., & Mandell, A. M. 2011, Natur, 475, 206
Ward, W. R. 1981, Icar, 47, 234
Wasson, J. T., & Kallemeyn, G. W. 1988, RSPTA, 325, 535
Webber, W. R. 1998, ApJ, 506, 329
Weidenschilling, S. J. 1977, MNRAS, 180, 57
Wood, B. J., Smythe, D. J., & Harrison, T. 2019, AmMin, 104, 844
Zhu, W., & Dong, S. 2021, ARA&A, 59, 291